ISSN: 2834-359X

Research Article

Journal of Plasma Chemistry and Plasma Processing Research

Optimization of Magnetic Dielectric Nanocomposites Obtained by Facile and Low-Cost Fabrication for Effective Absorption of Electromagnetic Waves

F Heydari[1], S S Seyyed Afghahi[1]*, A A Ebrahimi Valmoozi[1] and Sayed Mohamed Bagher Bahrani[2]

[1]*Department of Materials Science and Engineering, Imam Hossein University, Iran*

[2]*Department of Metallurgy and Materials Engineering, Iran University of Science and Technology (IUST), Iran*

***Corresponding Author**
S S Seyyed Afghahi, Department of Materials Science and Engineering, Imam Hossein University, Iran.

Submitted: 2023, Dec 15; **Accepted:** 2024, Feb 12; **Published:** 2024, Feb 16

Citation: Heydari, F., Afghahi, S. S. S., Valmoozi, A. A. E., Bahrani, S. M. B. (2024). Optimization of Magnetic Dielectric Nanocomposites Obtained by Facile and Low-Cost Fabrication for Effective Absorption of Electromagnetic Waves. *J Pla Che Pla Pro Res, 5*(1), 01-23.

Abstract

This work presents the synthesis of Fe_3O_4 nanoparticles (FNPs) and nanocomposites (NCs) of FNPs and functionalized carbon nanotubes (CNTs) at varying weight ratios for application in 8–18 GHz electromagnetic waves (EMW) absorbers. Their dielectric, magnetic, and structural characteristics were also examined. To create the desired NCs, CNTs are first mixed with FNPs at various weight ratios. The magnetic properties of the samples were ascertained using a vibrating sample magnetometer, and the dielectric properties of all the samples were examined by a vector network analyzer at room temperature after the crystal structure of the samples was determined by X-ray diffraction, surface morphology, and elemental analysis by scanning electron microscopy, energy dispersive spectroscopy, and Fourier transform infrared spectroscopy. Fe_3O_4@CNTs NCs in six different weight ratios (NC_1-NC_6) were prepared. Sample NC_3, with a thickness of 2.25 mm, exhibited the greatest loss in the X band, measuring -27.07 dB, out of all the samples. Additionally, the NC_4 sample which has a thickness of 5.00 mm, had the best loss, which came in at -38.21 dB in the Ku band. A data-driven method developed for multi-parameter optimization was then used to find out the optimal ratio weight ratio and sample thickness based on the experimental data. Samples with minimum reflection loss -34.1 dB (-41.5 dB), and others with effective bandwidth coving 69.0 % (71.4 %) in the X band (Ku band) were obtained.

Keywords: Microwave Absorption, Spinel, Ferrite, Dielectric, Fe_3o_4 Nanoparticles, CNTs, Nanocomposite

1. Introduction

Numerous applications in the fields of science, engineering, and the military can arise from studying the interaction of electromagnetic radiation (EM) with magnetic nanoparticles (MNPs) and their energy loss. Over the past ten years, a lot of research has been done in this area on MNPs, with an emphasis on materials that have large absorption bands, light weights, and high absorption rates. Therefore, metal- and alloy-based NCs have been the focus of research [1-4]. Magnetic and electric loss are part of the primary EMW loss mechanism. Graphite, graphene, carbon nanotubes (CNTs), and conductive polymers are examples of materials with electrical dissipation properties, while ferromagnets, ferrites, and carbonyl iron (CI) are examples of materials with magnetic dissipation properties [5-8]. Our absorption width will be small and weak if EM waves are only absorbed by one of these losses. Thus, in the field of microwave absorption, composites containing both magnetic and electric components are employed. Soft magnetic alloys have special qualities that make them ideal for absorbing electromagnetic fields in the GHz range. Wave absorption may be possible with composites of these materials that include conductive polymers, dielectric materials, or various forms of carbon. Studies on ferrite-based composites as microwave absorbers have been widely conducted in recent years.

Chi et al, examined the characteristics of NCs containing CNTs and cobalt ferrite in terms of their microwave absorption [9]. Because of the improved matching of dielectric and magnetic dissipation, these NCs, which were created using a chemical coprecipitation method exhibited superior microwave absorption properties compared to pure nanotubes and pure cobalt ferrite. At a frequency of 9 GHz, these NCs reflection loss (RL) was -18 dB.

The EM characteristics and microwave absorption of CNTs filled with cobalt ferrite were examined by Zhuo et al [10]. In this study, using a coating with a thickness of 1 mm, the researchers were able to achieve an RL below -10 dB in the 10.8–14.2 GHz frequency range. These composites' improved microwave absorption characteristics are correlated with both dielectric and

magnetic losses. The microwave absorption peak of CNT-epoxy composites was shifted to higher frequencies by the addition of cobalt ferrite NPs. A significant interface between cobalt NPs and the inner surfaces of cobalt-containing CNTs has been seen when compared to CNTs without cobalt.

In the field of silicone epoxy, Ging et al, studied the absorption characteristics of microwaves and CI particles as magnetic absorbers and carbon fibers as dielectric absorbers [11]. When the quantity of carbon fibers increased and the amount of CI remained constant, the electrical permeability rose but the magnetic permeability remained unchanged within the frequency range of 2-18 GHz. In this study, the researchers obtained an RL below -5 dB in a thickness of 1 mm, independent of the carbon content (2–6% wt.%) in the 4–18 GHz frequency range. Additionally, an RL of less than -10 dB has been found at a thickness of 1-3 mm. This has caused the composition's relative linearity (RL) to shift to lower frequencies as the thickness and carbon fiber content have increased.

In the frequency range of 2–18 GHz, Guoxiu et al. investigated the advanced electromagnetic properties of absorbers containing CNT and CI powders [12]. The electrical conductivity, electrical permittivity, and dielectric loss of CI/CNT composites were greater than those of CI. Between the various weight percentages of the nanotubes, the RL in the thickness range of 1.2-2.5 mm at a frequency range of 6.4-14.8 GHz was lowered to -20 dB in 2.2 wt.% CNTs. The findings show that low-weight percentages of thin-film CNT adsorbents can be produced, as well as light-weight materials with superior absorption capabilities.

Wei et al, used the spray method to examine the EM absorption characteristics of composites that included CI and flaky graphite as absorbents in polyurethane [13]. In this paper, the EM characteristics of CI/sheet graphite composites were investigated in relation to frequency and different weight percentages of graphite. It has been reported that altering the weight percentage of graphite in the 18–4 GHz frequency range can change the absorption properties of microwave waves, and increasing the amount of graphite in the composite can increase the EM parameters. The findings show that in a 1.2 mm thick coating with 50% weight percent CI and 75% weight percent graphite, RL was less than -10 dB in the 5.23–8.23 GHz frequency range in another study. In the 4-18 GHz range, Wei et al, looked into the EMW absorption characteristics of coatings containing cobalt ferrite and CI particles [14]. They created coatings with varying weight percentages of cobalt ferrite and CI particles as absorbents and aliphatic polyurethane resin as a base in order to achieve this. The RL results demonstrated that the cobalt ferrite-containing coatings have excellent absorption in the 18–12 GHz frequency range, with RL less than -10 dB Furthermore, hybrid coatings exhibit better absorption characteristics than coatings that solely contain cobalt ferrite and CI particles as absorbers the most efficient method of expanding the absorption bandwidth.

The microwave absorption characteristics of composites with CI particles in the silicone resin polymer matrix were studied by Zhao et al [15]. The spray method was used to create these composite materials. In the frequency range of 5–18 GHz at 0.8 mm thickness, the RL was less than -5 dB It has been observed that the frequency corresponding to maximum absorption shifts into the low frequency range as the thickness of the absorbent material increases.

Cui et al, used a two-step oxidative polymerization of aniline monomers in the presence of Fe_3O_4 microspheres and the wave method to successfully prepare composites consisting of Fe_3O_4 microspheres (FMS) and polyaniline (PANI), or FMS/PANI. Each step of the two-step polymerization process employed ammonium persulfate and Fe^{+3} as oxidants [16]. They also looked into the Fe_3O_4/PANI composite's microwave absorption characteristics between 2-18 GHz. Each step of the two-step polymerization process uses ammonium persulfate and Fe^{+3} as oxidants. The two-step oxidative process has been shown to be primarily responsible for the morphology of these composites. As a result, the first stage primarily produces aniline oligomers oxidized by Fe^{+3}, while the second stage yields "egg-shaped" PANI grains. Permeability is shown to be modified by embedding (FMS) in polymer matrices. Furthermore, the composite containing equal parts FMS and PANI, or FMS/PANI50, exhibits a very strong RL over a broad frequency range that is controllable by the absorber's thickness.

Liu et al, developed new sandwich structures of graphene, Fe_3O_4 and PANI using TiO_2 nanosheets using hydrothermal and polymerization techniques [17]. The VSM findings demonstrate the superparamagnetic behavior of the NPs. X-ray diffraction, transmission electron microscopy, and field emission scanning electron microscopy were used to characterize the structure and morphology. Images captured by electron microscopy demonstrate that TiO_2 nanosheets form sandwich structures by growing primarily vertically and randomly oriented on top of Fe_3O_4/PANI/graphene. In the 18–2 GHz frequency range, the absorption characteristics of the EMW of Fe_3O_4/PANI/graphene/TiO_2 nanosheets with 50% by weight of paraffin were studied. With a thickness of 1.6 mm, the NCs maximum RL is -41.8 dB at 14.4 GHz. As a result, Fe_3O_4/PANI/graphene/TiO_2 nanosheets have improved EMW absorption qualities and show promise as EMW absorbers.

Tawfik et al, used a co-precipitation method to combine Fe_3O_4 nanoparticles with PANI and activated carbon (AC). Fe_3O_4/AC/PANI NCs were produced at varying weight percentages (0.1-0.5 gr) by varying the mass of AC [18]. The very low composition of the AC crystalline phase was reported to be unmatched. The functional groups C-C and COOH vibrations have been used to detect the presence of AC. The benzoic ring and quinoid bond vibrations signal the presence of PANI. Furthermore, the existence of Fe-O functional groups from octagonal and tetragonal positions verified the presence of Fe_3O_4. Furthermore, the Fe_3O_4/AC/PANI NCs optical characteristics have been demonstrated by a decrease in absorption wavelength and an increase in energy gap. Remarkably, the Fe_3O_4/AC/PANI NCs absorption bandwidth expanded when the composition of AC increased.

Jiang and colleagues looked into powdered Coffee alloy. The Co0.4Fe0.6 sample has the highest magnetic permeability and electrical conductivity, according to an examination of its EM characteristics [19]. The Co0.4Fe0.6 sample with a thickness of 2.00 mm and a frequency of 1.15 GHz has the highest RL (-38.7 dB), according to the results of the RL study. Van Heng et al. investigated powdered CoNi alloy [20]. Five ratios are used in the liquid phase reduction method to create CoNi alloy. The powders in all five ratios are on a nanometer scale and have a spherical shape, according to SEM images. Furthermore, Co:Ni has the highest electrical conductivity and magnetic permeability at a ratio of 1:2, according to an analysis of its electromagnetic properties. The sample with the highest RL value of -32 dB is the 1:2, Co: Ni sample with a thickness of mm2 and a frequency of 3.8 GHz, according to the results of the RL study. Zhang et al, investigated how lessening chemical oxidation could improve microwave absorption in core-shell composites containing graphene and Fe_3O_4/polypyrrole (PPy) [21]. According to their research's findings, the maximum RL at a 7.1 GHz frequency is -25.1 dB at a thickness of 4 mm. Furthermore, a minimum of -10 dB is observed for the RL bandwidth in the frequency range of 13-18 GHz.

Core-shell composites (PANI/CIP, PANI/Fe_3O_4, and PANI/CIP/Fe_3O_4) were assessed by Zhifuhi et al, between 0.5 and 18 GHz [22]. The samples with the highest saturation magnetization and coercive force are PANI/Fe_3O_4, PANI/CIP/Fe_3O_4, and PANI/CIP, according to the VSM analysis results. SEM pictures additionally demonstrate the spherical nature of all three composites. The PANI/Fe_3O_4 and PANI/CIP/Fe_3O_4 and PANI/CIP samples have the best absorption in the frequency range of 8–12 GHz and 2.00 mm thickness, respectively, according to the absorption results. Using a core-shell model with Fe_3O_4 NPs and a PANI conducting polymer as the shell material and Fe_3O_4 NPs as the core, Qiu et al. investigated the enhancement of microwave absorption. The 300 nm-size Fe_3O_4 material is produced by the thermal solvent method, and PANI is deposited on Fe_3O_4 in varying thicknesses using the in-situ polymerization method. The aim of this study is to examine the loss of microwave radiation at various PANI to Fe_3O_4 ratios. Additionally, the SEM pictures of every sample demonstrate that every sample's particles are round. All the samples were investigated for their magnetic properties and Fe_3O_4 has the highest magnetism. The amount of saturation magnetization decreases with increasing PANI to Fe_3O_4 ratio. For every sample, the loss of microwave waves between 2-18 GHz was analyzed at a constant thickness of 2.00 mm. At a frequency of 15.6 GHz, the best-reported absorption is -37.4 dB; the loss value of Fe_3O_4 and PANI alone is weak. Furthermore, for this thickness ratio, a maximum loss of 2.5 mm has been reported [23,24].

The citrate nitrate method was used in this work to prepare hierarchical structures made of Fe_3O_4 NPs. Subsequently, under ultrasonic waves, CNTs and Fe_3O_4 NPs were mixed at various weight ratios to create Fe_3O_4/CNT NCs. Lastly, an examination was conducted into their structural, magnetic, and dielectric characteristics. In fact, the citrate-nitrate method which has several benefits, such as simple synthesis, inexpensive cost, and industrialization potential was employed for the first time to prepare these NPs to absorb microwave waves. Based on maximum RL and absorption bandwidth, the results indicate that the fabricated NCs EMW absorption has increased. The NC3 (2.25 mm, RL = -27.07 dB) and NC4 (5.00 mm, RL = -38.21 dB) samples have the highest levels of RL in the X and Ku bands, respectively. The addition of CNTs to Fe_3O_4 NPs increases the maximum RL and absorbable bandwidth of the samples in the 8-18 GHz frequency range, according to the results of RL measurements. A data-driven method was also applied to adjust the weight ratio of the different additives and the sample thickness in order to achieve the highest possible microwave absorption performance based on the experimental data.

2. Experimental

2.1. Materials

The Fe_3O_4@CNT NCs are made with iron nitrate ($Fe(NO_3)_3 \cdot 9H_2O$), citric acid ($C_6H_8O_7$), and carbon nanotubes (CNTs), all of which are obtained from Sigma Aldrich.

2.2. Preparation of Fe_3o_4 Spinel Ferrite NPs

In order to fully dissolve these materials, they were first combined with Fe $(NO_3)_3 \cdot 9H_2O$ and $C_6H_8O_7$ (ratio 1:1) in a minimum amount of water [24,25]. After that, we baked the prepared solution for 12 hours at 90 °C to ensure it was completely dry. After that, we take the dried material out of the oven and turn it into a powder, and the obtained powder is transferred into the crucibles and calcined for three hours at a temperature of 200 degrees Celsius. At the specified temperature, the salts finally break down and the desired phase forms [25-29].

2.3. Synthesis of Fe_3O_4/CNTs NCs

NCs containing dielectric material (CNTs) and Fe_3O_4 NPs were prepared at varying weight ratios of NC1, NC2, NC3, NC4, NC5, and NC6 in order to study the absorption properties of microwave waves. The simplest method for creating EMW covers is to physically combine magnetic particles and dielectric materials while applying ultrasonic waves. This method's industrial capability is developed by its quick construction time and ease of use. Fe_3O_4 NPs were mixed with dielectric material (CNTs) in various weight ratios with paraffin for this purpose, and the mixture was then molded.

2.4. Characterization

The structures of the Fe_3O_4 NPs and Fe_3O_4/CNT NCs were determined using an XRD device, Cu-Kα (λ=1.540 Å). Additionally, a FESEM-EDAX device was used to observe the morphology and identify the elements of the Fe_3O_4/CNT NCs compounds. The functional groups of the Fe_3O_4/CNT NCs were determined by FTIR. A VSM device was used to check the magnetic properties of the prepared samples. Finally, the radar absorption of Fe_3O_4/CNT NCs was investigated using VNA.

3. Results and Discussion

3.1. Structural and Morphological Properties

Figure 1. displays the XRD patterns of CNTs, pure (Fe_3O_4 NPs), and NCs NC1-NC6. Structural characterization of XRD patterns, including crystal structure type and space group, as

well as cell lattice parameter calculation, were performed for pure, NC1–NC6 samples. The absence of additional reflection in the diffraction pattern indicates the formation of a pure phase. The values (hkl) corresponding to the spinel phase diffraction peak are specified in Figure 1. Plates (220), (311), (222), (400), (422), (511), and (440) are represented by the observed peaks. There is a preferential peak towards the (311) plane, suggesting that this direction is where the crystal order is more formed. Furthermore, in all samples, the distinctive diffraction peak at roughly 26° can be indexed to the graphitic carbon (002) plane. The peaks at 18.3°, 30.1°, 35.5°, 43.1°, 53.5°, 57°, and 62.7° can be easily identified by Bragg reflection, as can be observed from the NCs patterns: (220), (311), (222), (400), (422), (511), and (440), indexed in accordance with the standard card (JCPDS 01-075-0449). Notably, no impurity peaks were discovered. This suggests that Fe_3O_4/CNT NCs are formed. The intensity of the Fe_3O_4 diffraction peaks increases with increasing carbon nanotube concentrations, with the exception of the NC3 and NC6 samples. This indicates that the addition of carbon nanotubes has an impact on the average size of the Fe_3O_4 nanoparticles. Furthermore, in comparison to other composites, the peaks of NC3 and NC6 exhibit a slight shift toward a smaller angle, suggesting that a distinct compositional mode between Fe_3O_4 NPs and CNTs may occur in this instance.

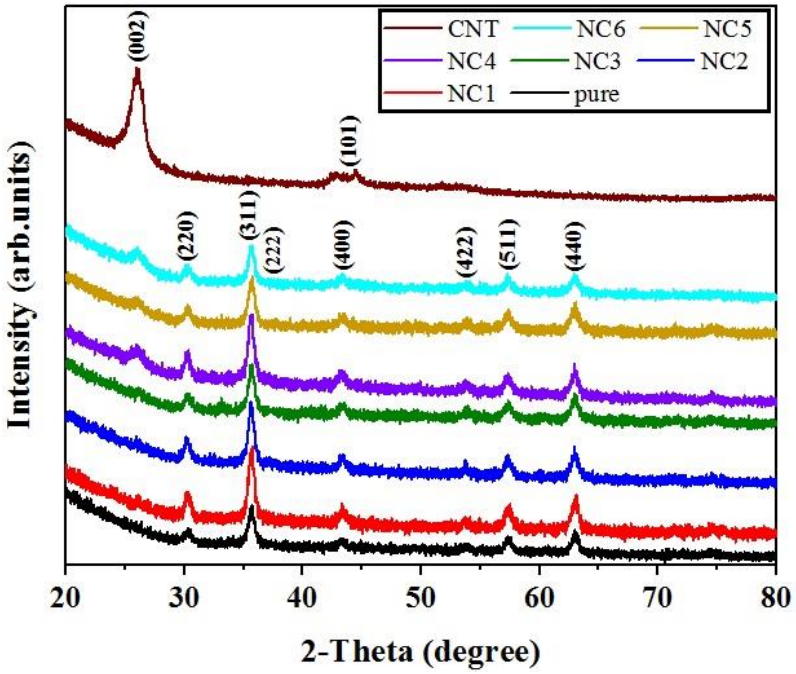

Figure 1: XRD Patterns of Pure CNTs, Pure Fe_3o_4 NPs, and Nc1- Nc6 NC's.

Xpert software package confirms the formation of cubic spinel structures with space groups ($Fd3\bar{m}$) without impurity phase. Table 1 lists the values of the lattice parameters, unit cell volume, crystal size determined by the H-W method, microstrain, theoretical density, experimental density, and porosity. Based on the location of the peak (311) in the X-ray diffraction patterns, the lattice parameter of the spinel structure of the samples was determined. The following formula yields the lattice parameter (a) for crystals with a cubic structure:

$$\frac{1}{d^2} = \frac{h^2+k^2+l^2}{a^2} \quad (1)$$

In this relationship, the Miller indices of crystal plates are h, k, and l, and the distance between plates, (d), is determined using Bragg's equation. The following relation is obtained by integrating Bragg's law λ=2dsinθ with relation (1):

$$\frac{4sin^2}{\lambda^2} = \frac{h^2+k^2+l^2}{a^2} \quad (2)$$

With every sample's peak location (311), the lattice parameter a has been determined. In addition, the following equation was used to determine the unit cell volume (V):

$$V = a^3 \quad (3)$$

The parameter of the network is a. Consequently, the value of the lattice parameter rises as the weight ratio of CNTs from the pure sample to the NC1 sample increases, as shown in Table 1. In other words, the lattice parameter rises as the amount of Fe_3O_4 NPs decreases and the amount of CNTs increases. Next, there is an increasing process of the lattice parameter from sample NC1

to sample NC3. The distribution of cations at tetrahedral and octahedral sites varies as a result of the non-uniform behavior of the lattice parameter brought on by the increase in CNT substitution. Considering that the points are nearer the fitting line when using the H-W method. Therefore, the crystallite size is determined by the H-W method. As a result, the following equation was used to determine the crystallite size using the H-W method and the lattice parameter:

$$D = \frac{1}{a} \tag{4}$$

Of course, there is consistency between the variations in lattice parameters and the variations in crystallite size. By applying the following equation to b (Intercept), microstrain (ε) was obtained:

$$(\frac{\varepsilon}{2})^2 = b \rightarrow \varepsilon = 2\sqrt{b} \tag{5}$$

For all samples, the theoretical density, or ρXRD, was calculated using the following formula:

$$\rho_{XRD} = \frac{8M}{N_A a^3} \tag{6}$$

NA is Avogadro's number, a is also the lattice parameter and M the molar mass of the Fe_3O_4 formula [29]. For all samples, the experimental density, or ρexp, was also determined using the following equation:

$$A \times d = V \rightarrow \rho = \frac{m}{V} \tag{7}$$

where A represents the cross-sectional area, d the sample's thickness, m the weight, and V the volume. P stands for porosity. Which, for all samples, it was measured using the relation (8) [30].

$$P = \frac{\rho_{\mathrm{XRD}} \times \rho_{\mathrm{exp}}}{\rho_{\mathrm{XRD}}} \times 100 \tag{8}$$

Sample	a (Å)	V (Å^3)	$D_{\mathrm{H\text{-}W}}$ (nm)	$\varepsilon \times 10^3$ (unitless)	ρ_{XRD} (g/cm^3)	ρ_{exp} (g/cm^3)	P (%)
Pure	8.344	581.07	9.86	6.08	5.29	5.10	3.64
NC1	8.351	582.47	12.30	4.83	5.28	5.09	3.54
NC2	8.346	581.42	10.99	4.68	5.29	5.10	3.59
NC3	8.347	581.70	9.87	5.10	5.29	5.08	3.84
NC4	8.353	582.86	10.59	3.40	5.27	5.08	3.71
NC5	8.345	581.16	10.96	4.50	5.29	5.10	3.65
NC6	8.346	581.47	9.36	3.86	5.29	5.10	3.67

Table 1: Values of the Lattice Parameter, Crystallite Size, Microstrain, XRD Density, Experimental Density, and Porosity as Well as Vibration Frequencies of the Samples

The $(\frac{\beta^*_{hkl}}{d^*_{hkl}})^2$ vs. $(\frac{\beta^*_{hkl}}{d^{*2}_{hkl}})$ plots in the H-W method for pure, NC1-NC6 samples are shown. In Figure 2, The H-W method is more accurate than other methods because the points are closer to the fitting line in this method [22,23].

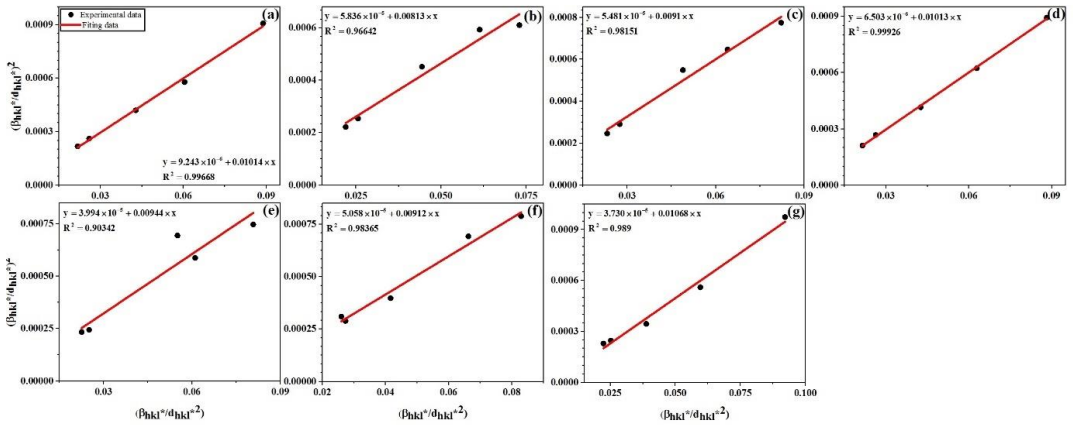

Figure 2: $(\frac{\beta^*_{hkl}}{d^*_{hkl}})^2$ versus $(\frac{\beta^*_{hkl}}{d^{*2}_{hkl}})$(h–w plot) for Samples (a) Pure, (b) NC1, (c) NC2, (d) NC3, (e) NC4, (f) NC5, and (g) NC6

To learn more about the precise microstructure and chemical makeup of the Fe3O4/CNT NCs, EDX and FESEM analyses were performed. In Figure 3(a), (b), FESEM images of pure samples (Fe_3O_4 NPs) are displayed. After drawing the Fe_3O_4 NPs size distribution diagram, the average particle size (DFESEM) was calculated by fitting the distribution of particle sizes with the normal logarithm distribution function in the following way:

$$P(d) = \frac{1}{d\sigma_d\sqrt{2\pi}} \exp\left(-\frac{1}{2\sigma_d^2} ln\left(\frac{d}{D_{FESEM}}\right)\right) \qquad (9)$$

35.65 nm is the average particle size. This method yields a larger particle size than what XRD data can provide. This could be because the NPs are made of multiple crystals with different orientations. This could be because the NPs are made of multiple crystals with different orientations. Image an of Figure 3 shows the development of nanoscale clumps. One could almost argue that the synthesized nanoparticles have a spherical shape based on Figure 3b. Pictures a and b of Figure 3 demonstrate the multifaceted nature and degree of agglomeration of the Fe_3O_4 NPs. Their high surface and magnetic interactions may be the cause of this agglomeration. Furthermore, the smooth surface and open tip of the empty CNTs can be observed from the FESEM images of Figure 3(c), (d).

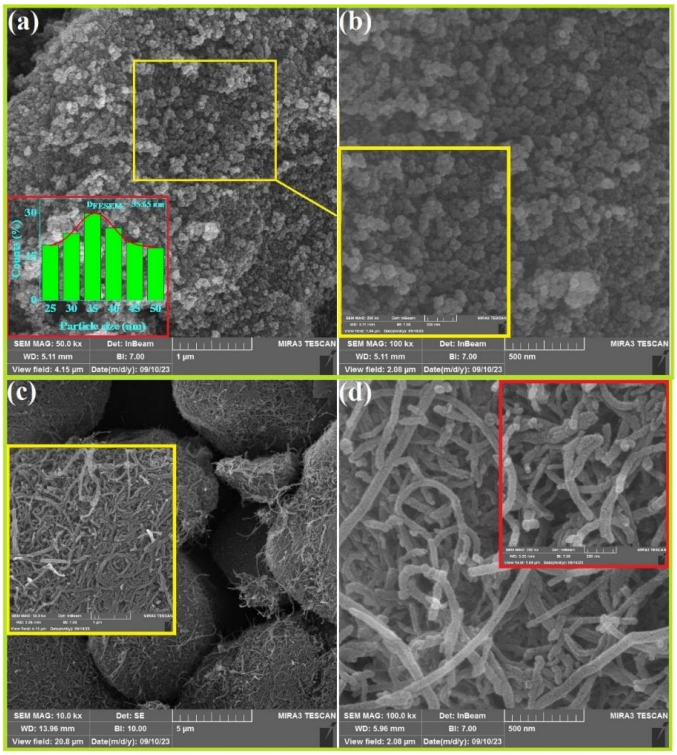

Figure 3: Shows the Normal Log Distribution of Fe_3o_4 Nps Along with Their Fit for Various Magnifications (A) and (B); it also Shows the Fesem Images of the Powdered Cnts Under Various Magnifications (C) and (D).

FESEM images of the NC1-NC6 NCs are displayed in Figure 4. The nanotubes' surfaces are not perfectly smooth. The majority of carbon nanotubes are fully covered in Fe_3O_4 NPs, as evidenced by the light and dark contrast, indicating the successful preparation of Fe_3O_4/CNTs NCs. The presence of C, N, O, and Fe elements (gold signals from the conductive coating) in the synthesized NCs EDX spectrum provides additional evidence that Fe_3O_4 nanoparticles are successfully embedded in or on CNTs. It is evident from comparing the FESEM pictures of the NCs that the coating density and particle size of the Fe_3O_4 NPs can vary depending on how much CNTs are added. The majority of the magnetic nanoparticles (NPs) are evenly distributed on the CNTs' surface; however, a small number of particles are visible inside the NC3 sample's hollow cavity (Figure 4(e), (f)).

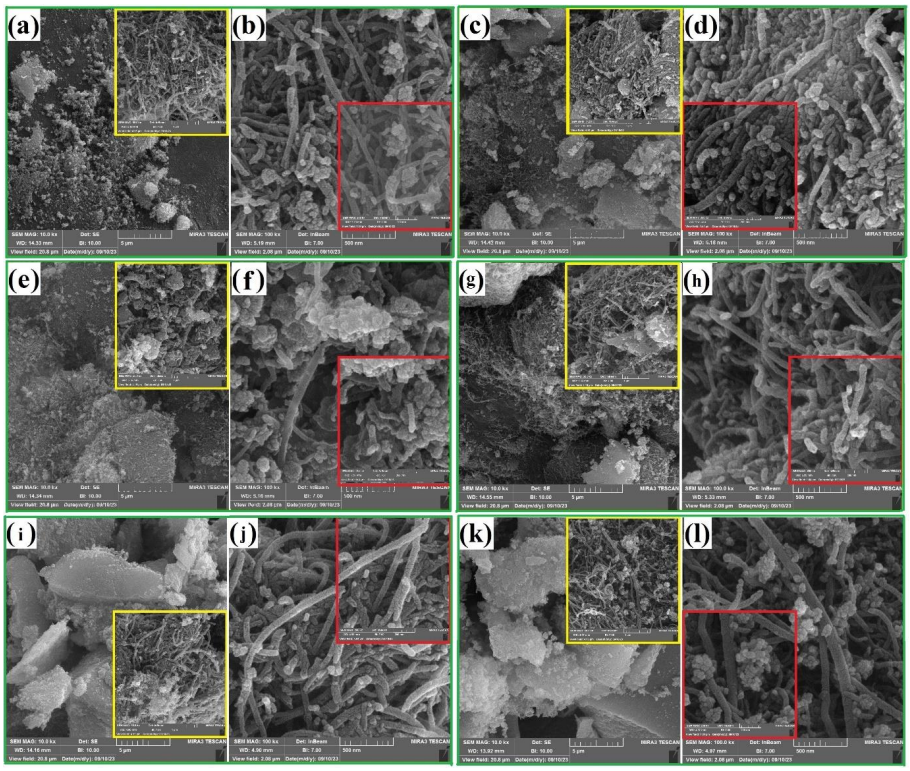

Figure 4: FESEM Images of Prepared NCs (A) and (B) NC1, (C) and (D) NC2, (E) and (F) NC3, (G) and (H) NC4, (I) and (J) NC5, (K), (L) NC6

Figure 5(a), (b), (c), and (d) and Figure 5(e), (f), (g), and (h) show TEM images of CNTs and NC3 NC, respectively. The light and dark contrast shows that the majority of the carbon nanotubes (CNTs) are entirely covered in Fe_3O_4 nanoparticles, confirming the previously mentioned uneven surfaces of the nanotubes and the successful synthesis of the Fe_3O_4/CNTs NCs. The amount of CNT added can alter the coating density and particle size of the Fe_3O_4 NPs, as can be seen by comparing the SEM and TEM images of the NPs. A portion of the magnetic NPs can be seen inside the NC3 sample's hollow cavity, but the majority of the particles are almost evenly distributed across the surface of the CNTs.

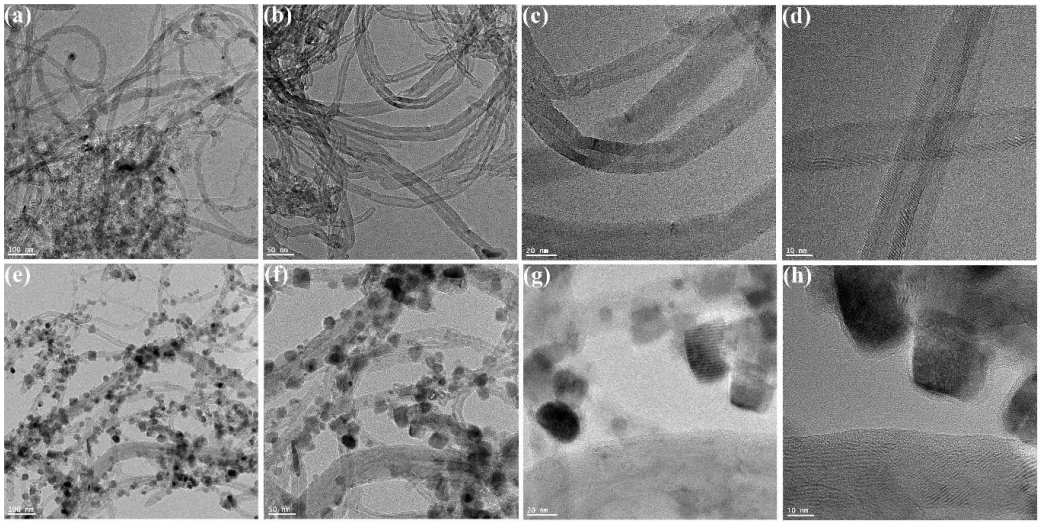

Figure 5: TEM Images (A), (B), (C), (D) of CNTs and (E), (F), (G), (H) Sample NC3.

The pure, CNTs, and NC3 samples underwent WDX analysis to further verify the presence of various elements on the modified electrode surface. which contain elements of Fe, O, C, and N. Furthermore, Figure 6 displays the distributions of Fe, O, C, and N. In addition to FESEM microscopy, EDX was employed. An effective method for identifying the type and purity of an element is to use EDX. The elemental analysis spectra of the pure, CNTs, and NC1 samples are displayed in Figure 6(a), (b), and (c), respectively. Figure 6(a) shows the energy lines for O and Fe elements. In Figure 6(b), the energy lines of C, N and O elements can be seen. Figure 6 (c) also shows the energy lines related to C, N, O and Fe elements.

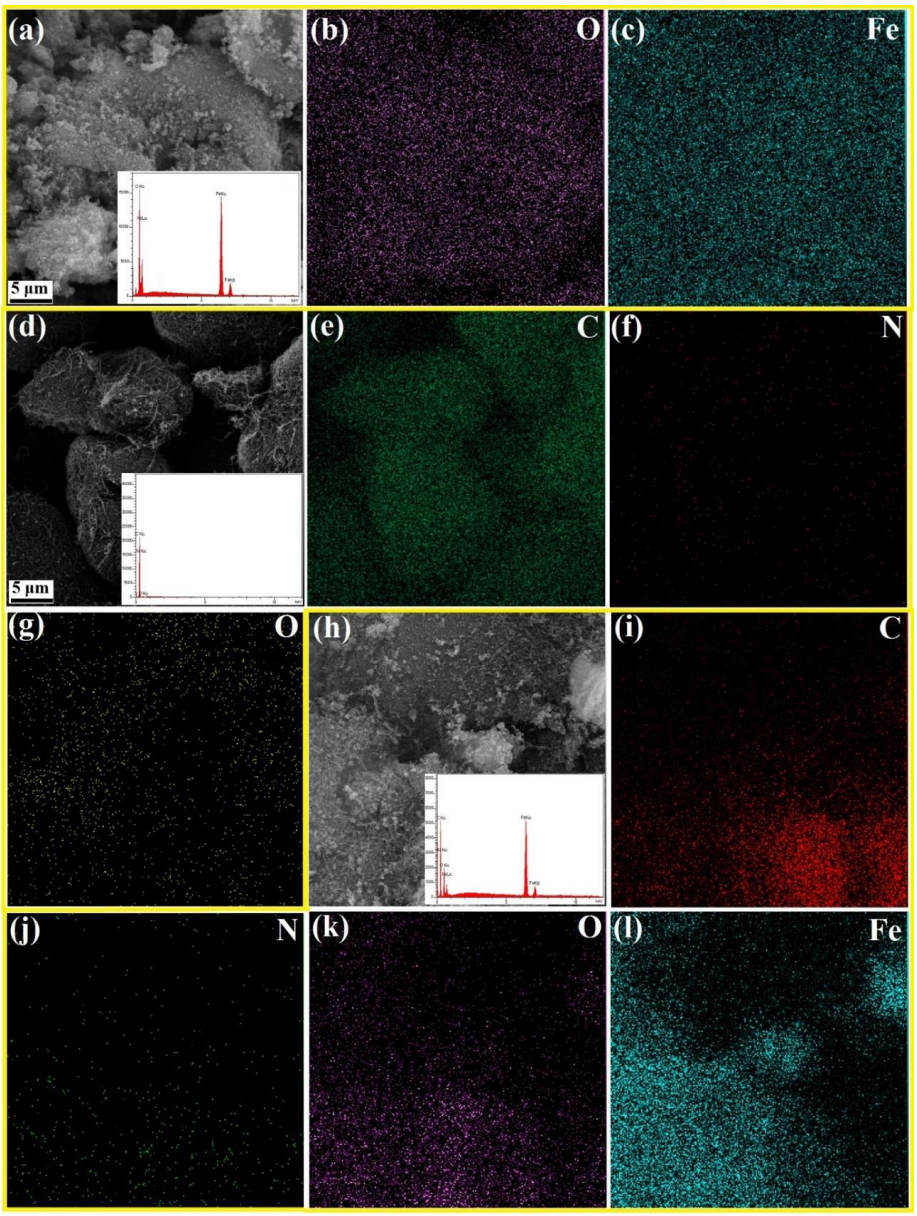

Figure 6: (A), (B), (C) EDS Map for Pure Sample, (D), (E), (F) For CNTs and (G), (H), (I), (J), (K), (L) for NC3 Sample

3.2. Infrared Spectroscopy

Figure 7 displays the infrared spectra of all samples in the 400 cm-1 to 4000 cm^{-1} wavenumber range. Like all spinel ferrites, Fe_3O_4 NPs exhibit two strong absorption bands in the 400 cm^{-1} to 600 cm^{-1} range in their infrared spectrum. The O-M intrinsic vibrations in the octahedral position are represented by the υ_2 frequency band at approximately 400 cm^{-1}, and the O-M intrinsic vibrations in the tetrahedral position by the υ1 frequency band at roughly 600 cm^{-1} [29]. These two bands are primarily associated with Fe-O vibrations in this paper. Furthermore, the O-H stretching brought on by the carboxyl group on the surface of CNTs-COOH is linked to the absorption bands at roughly 617 cm^{-1} and 3415 cm^{-1} of empty CNTs, which can aid in the coating of CNTs. The C-H stretching vibrations, which also originate from the CNT surface, are responsible for the bands at 2921 cm^{-1} and 2843 cm^{-1} [30]. O-H bending vibrations or C=O stretching vibrations are responsible for the absorption at 1628 cm^{-1} [31-33]. Its peak occurs at about 1036 cm^{-1} and is caused by the C-C skeleton vibrating. The presence of Fe_3O_4 is further confirmed by the 585 cm^{-1} band found in the spectra of all NCs, which is associated with the Fe-O bond's stretching vibration [34].

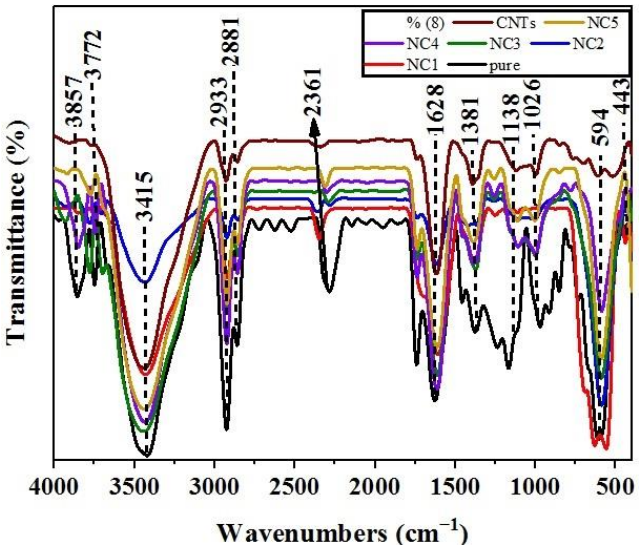

Figure 7: FT-IR Spectra of Pure, NC1- NC6 Samples

3.3. Magnetic Properties

Figure 8 displays the magnetic hysteresis loops for the NC1–NC6 and pure samples. This curve can be used to determine changes in the saturation magnetization of the samples (MS), the coercive field (HC), the residual magnetization (Mr.), etc. Furthermore, all room temperature magnetic resonance loops exhibit clear, smooth S-like curves and pass through the coordinate origin, as illustrated in Figure 8. Which demonstrates the advantageous superparamagnetic properties of all NCs [36]. The MS for of pure, NC1, NC2, NC3, NC4, NC5, and NC6 samples is equal to 49.09, 47.46, 35.70, 33.79, 32.65, 31.74, and 28.83 emu/g, respectively. The larger particle size of Fe_3O_4 NPs indicates a larger saturation magnetization, based on the XRD and VSM results. That surface disorder or spin tilt are responsible for the samples' low saturation magnetization [35-37]. However, the lower loading density of Fe_3O_4 nanoparticles compared to carbon nanotubes in nanocomposites is primarily the main reason for the lower magnetization of nanocomposites [38]. In general, the average grain size and the amount of Fe_3O_4 nanoparticles loaded in nanocomposites have a significant effect on the MS values of the samples.

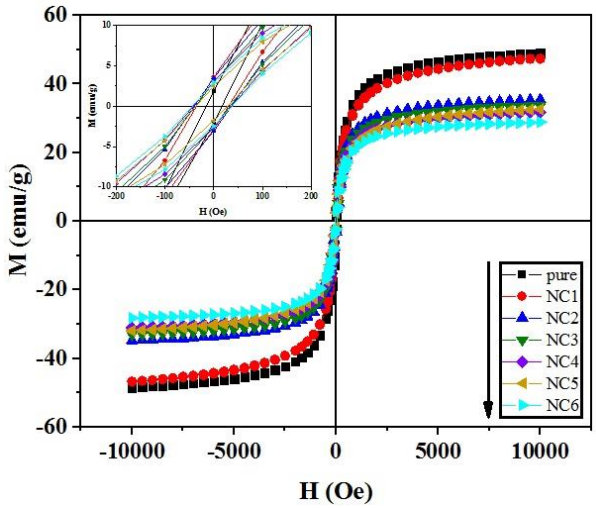

Figure 8: Magnetization Curves as a Function of the Magnetic Field for Pure, NC1-NC6 Samples At 300 K

Only spin processes are left at sufficiently high conducted field (H>>HC). As a result, the law of approach to saturation (LSA) is used to fit the M curve in terms of H [26]. The following is the LSA:

$$M = M_S\left(1 - \frac{a}{H} - \frac{b}{H^2}\right) + \chi H \qquad (10)$$

Magnetization in the H field is denoted by M(H). The following defines the fitted parameters: Anisotropy coefficients a and b for MS, assuming that the Berloni functions equal one. Shape anisotropy, magnetoelastic anisotropy, surface anisotropy, and magneto crystalline anisotropy are the energies that make up this anisotropy, and χ is the magnetic susceptibility. Figure 9 displays the fitting diagram for the samples. As mentioned earlier, the decrease in the weight ratio of Fe_3O_4 nanoparticles compared

to carbon nanotubes is the reason for the decrease in the magnetic values of the samples. The exchange interaction between the particles in these samples decreases as the particle size increases, which also lowers the overall magnetization. Various magnetic properties, such as H_C, M_S, M_r., magneto crystalline anisotropy constant (K), shape anisotropy (H_d), the square ratio of the remanence curve ($M_r./M_S$) and crystalline anisotropy field (H_a) were calculated using the residual loop of the samples. Particle size, porosity, structure shape, and magneto crystalline anisotropy are a few of the variables that affect the samples' residual curves [39].

The pure sample has a higher saturation magnetization than the other samples, as shown by Table 2's results. The coercive field and remanent magnetization (Mr.) change processes are comparable to one another. The documented articles state that a structure is multidomain if the relative density ratio is less than 0.5 and single-domain if it is greater than 0.5. The samples have a multi-domain structure based on Mr./MS values in Table 2 [40]. The pure sample grains differ from the other samples in terms of size and shape, as indicated by the FESEM results. As such, we anticipate that its magnetic characteristics will differ from those of other samples. Table 2 shows that the pure sample's coercive field is smaller than the other samples. Eq. 12 and Table 2 indicate that the anisotropy field and magneto crystalline anisotropy constant are two possible causes of this reduction. However, there is less anisotropy because the other samples are smaller in size than the pure sample. Furthermore, the cubic NPs of the other samples have a different shape than the spherical NPs in the pure sample. Which explains why the other samples' shape anisotropy is less than that of the pure sample. We anticipate that the pure sample will have a significantly lower coercive field than the other samples based on formula 13.

$$H_a = \sqrt{15b} \tag{11}$$

$$K = \frac{H_a M_S}{2} \tag{12}$$

$$H_C = 0.48(H_a - H_d) \tag{13}$$

Using saturation magnetization M (emu/g) and molecular weight MW (gmole-1), the magnetic moment values of all samples were computed in terms of the Bohr magneton using the following formula [41].

$$\mu_{f.u.}(\mu_B)\frac{M\left(\frac{emu}{g}\right)MW(gmol)^{-1}}{\mu_B\left(\frac{J}{T}\right)\times N_A(mol^{-1})\times 10^3}\left(\frac{J}{T}\right) = \frac{M\left(\frac{emu}{g}\right)\times MW(g)}{5585} \tag{14}$$

where $\mu_B = 10^{-24} \times 9.274$ (J/T) (Bohr magneton) and $N_A = 10^{23} \times 6.022$ mol^{-1} (Avogadro's number). The saturation magnetic change is dependent on two factors: unit cell volume (Vcell) and grain size. Table 2 shows how MS decreases with decreasing grain size.

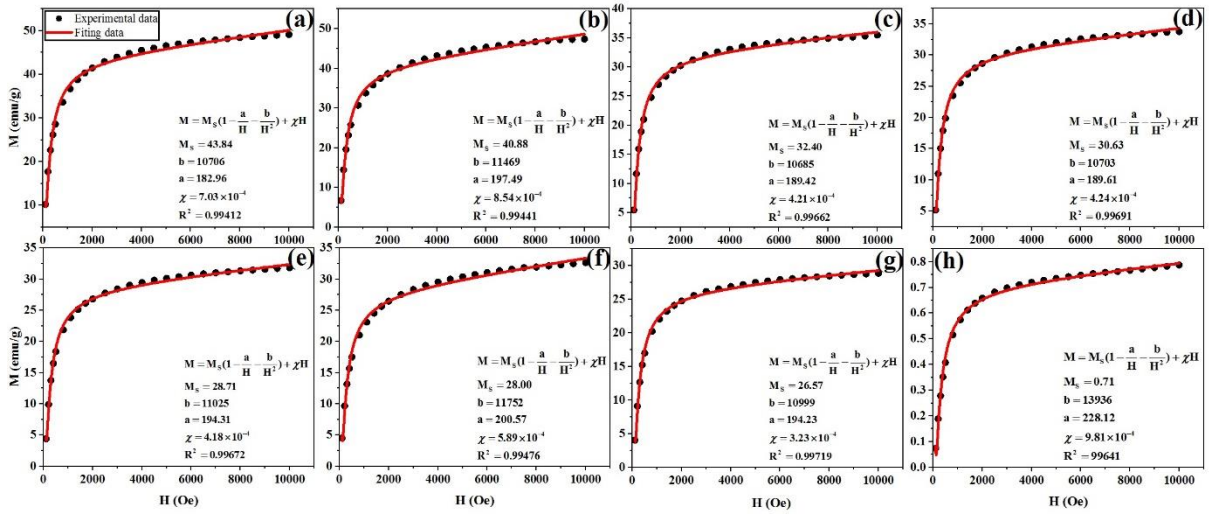

Figure 9: The LSA Fitting for Pure, NC1- NC6 Samples

sample	M_r (emu/g)	H_c (Oe)	M_s (emu/g)	$\mu_{f.u.}$ (μ_B)	M_r/M_s	$b*10^4$ (Oe^2)	a (Oe)	$K*10^3$ (erg/cm^{-3})	χ (emu/gOe)	H_a (Oe)
pure	1.86	17.24	43.84	2.04	0.03	10.70	182.96	19.76	7.03×10^{-4}	80295
NC1	3.63	31.15	40.88	1.96	0.07	11.46	197.49	20.40	8.54×10^{-4}	86017
NC2	3.52	37.47	32.40	1.47	0.09	10.68	189.42	14.24	4.21×10^{-4}	80137
NC3	2.94	33.89	30.63	1.40	0.08	10.70	189.61	13.56	4.24×10^{-4}	80272
NC4	2.99	37.71	28.71	1.32	0.09	11.02	194.31	13.16	4.18×10^{-4}	82687
NC5	2.45	28.72	28.00	1.35	0.07	11.75	200.57	14.38	5.89×10^{-4}	88140
NC6	2.93	37.48	26.57	1.19	0.10	10.99	194.23	11.92	3.23×10^{-4}	82492

Table 2: Saturation magnetization (M_S), remanence magnetization (M_r.), the square ratio of remanence curve (M_r./M_S), magnetic coercivity (H_c), crystalline anisotropy field (H_a), magneto crystalline anisotropy constant (K) and Magnetization fitting lines (M_S), anisotropy constants *a, b* and *x*

3.4. Microwave Absorption Properties of Prepared Materials

The response of pure, NC1-NC6 samples to microwave under X and Ku bands is measured by measuring the real and imaginary parts of their electrical permittivity and magnetic permeability. Using a Keysight E5063A ENA Vector Network Analyzer (VNA) in the 8–18 GHz frequency range, this measurement was carried out. Using this method, the real and imaginary parts of magnetic permeability and electrical permittivity are obtained by measuring the scattering matrix coefficients. Then, in the 8–18 GHz range, RL and the sample's absorption rate are computed using MATLAB software. The following relationships are used to express a material's magnetic permeability and electrical permittivity:

$$\varepsilon = \varepsilon' - i\varepsilon \tag{15}$$

$$\mu = \mu' - i\mu' \tag{16}$$

The symbols ε and ε' denote the electric field's electrical capacity and the existence of dielectric loss, respectively, while μ and μ' signify the magnetic field's energy storage and the presence of magnetic losses. The real part of the electrical permittivity diagram for the pure NC1–NC6 samples is shown in Figure 10(a), (b). That these samples have been investigated under X, Ku bands. The values of ε' for the pure, NC1, NC2, NC3, NC4, NC5, and NC6 samples are 3.32, 5.38, 7.67, 10.04, 8.77, 11.07, and 11.49, respectively, as shown in Figure 11(a). The values of ε' for the pure samples NC1, NC2, NC3, NC4, NC5, and NC6 are 3.47, 4.42, 5.61, 7.52, 7.86, 9.05, and 11.78, respectively, as shown in Figure 10(b). The pure sample has the lowest ε' value among these samples, while the NC6 sample has the highest ε' value.

Experience has demonstrated that creating an appropriate absorber cannot be accomplished by using a material that is merely magnetic or dielectric. To create a magnetic/dielectric nanocomposite, we combined magnetic iron oxide NPs (Fe_3O_4) with carbon nanotubes (CNTs) at various weight ratios. These nanocomposites are discussed in this paper under headings NC1–NC6. In addition, Figure 10(c), (d) corresponds to the imaginary part of electrical permittivity diagram of pure, NC1-NC6 samples in X and Ku bands. NC3 and NC6 Samples have the highest values of ε", as shown in Figure 10c, d. Figure 11c shows that a peak under the X band appears in NC3-NC6 samples as the CNT weight ratio increases. Which, at a frequency of 10.20 GHz, corresponds to the sample NC3 and has the highest value and the intense peak. The NC6 sample has the highest value of ε" under the Ku band. Naturally, there are tiny peaks in various frequencies here as well. Peaks are also present here because of the dielectric material's polarization and the electric field-induced interface between the dielectric and magnetic nanoparticles.

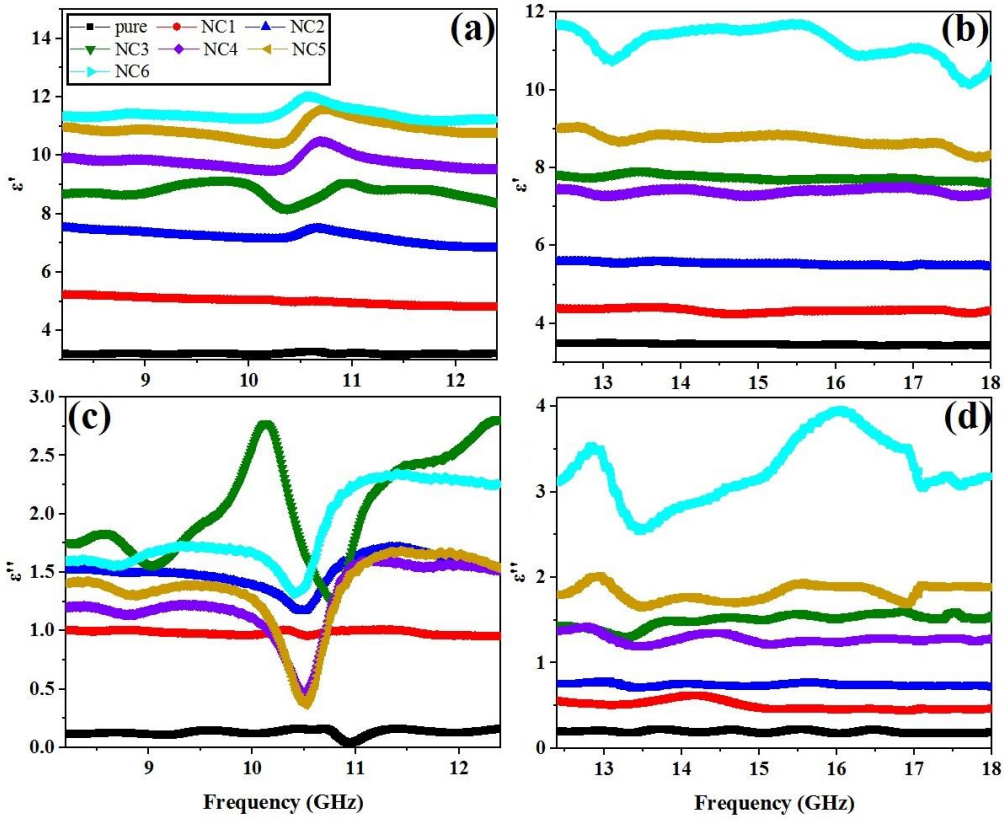

Figure 10: Diagrams of (A) Real and (C) Imaginary Parts of Permittivity Under the X Band, (B) Real and (D) Imaginary Parts of Permittivity Under the Ku Band for Pure, NC1-NC6 Samples

Figure 11(a), (b), shows the Cole-Cole plots for pure, NC1-NC6 samples. The NC3 sample has two Cole-Cole semicircles under the X band. Compared to other samples, it also has more values and bigger semicircles. The NC6 sample has two Cole-Cole semicircles for the Ku band, and these semicircles and values are larger than those of the other samples. Stated differently, these Cole-Cole semicircles suggest that these nanocomposites experience several Debye dielectric relaxations.

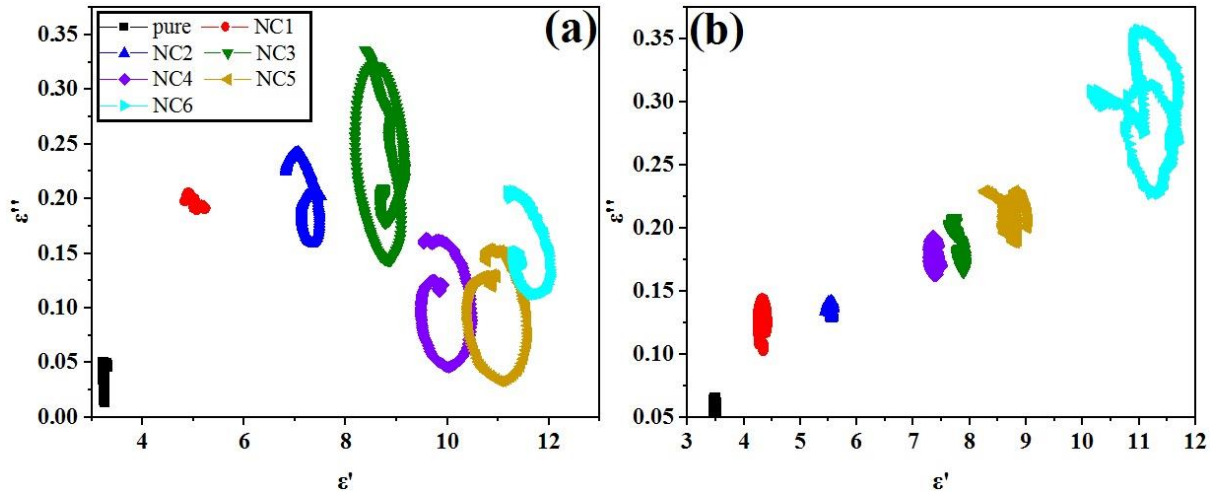

Figure 11: Cole-Cole Semicircles for Pure, NC1-NC6 Samples Under (A) X, (B) Ku Bands

The dependence of the magnetic permeability coefficient on the frequency is shown in Figure 12. According to Figure 12(a), (c) which is under X band, it can be seen that sample NC3 has the highest value of μ' and μ". As seen in Figure 12(b), (d), μ' and μ" for Ku band samples show a range of behaviors that are relatively close to each other. According to Figure 12b, d samples NC1, NC2, NC4, NC5, NC6 have higher μ' values than other samples. We find that when the frequency rises, samples experiences a gradual downward trend. We will look into mechanisms that cause magnetic loss, including eddy currents, magnetic resonance, and movement of the wall of the magnetic domains. There is a loss of wall motion of the magnetic domains

in multi-domain materials at frequencies ranging from 1 to 100 MHz [42]. The nanoparticles in this case are single- or multi-domain. Furthermore, since the applied frequency is in the gigahertz range, it is not possible for this kind of mechanism to be the primary cause of loss in these samples.

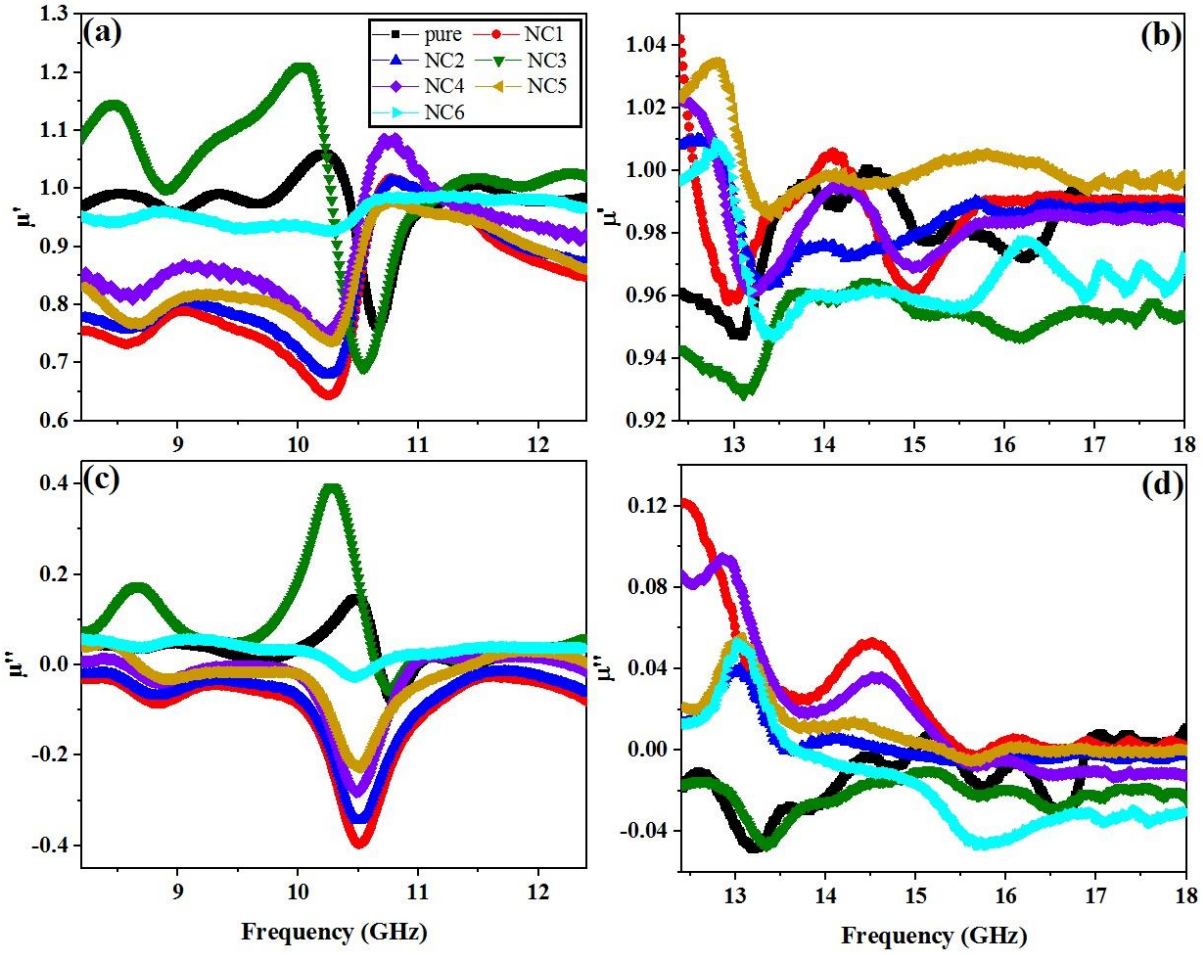

Figure 12: Diagram of the (A) μ' and (C) μ'' Under X Bands, Diagram of the (C) μ' and (D) μ'' Under Ku Bands Related to Pure, NC1-NC6 Samples

If eddy current losses are the only source of magnetic losses. The relationship that follows ought to hold steady despite the frequency change:

$$C_0 = \mu''(\mu')^{-2} f^{-1} \tag{17}$$

The effect of eddy current loss on μ' is as follows:

$$\mu'' = \frac{2\pi\mu_0(\mu)^2\sigma d^2 f}{3} \tag{18}$$

Equation (18) states that the electrical conductivity (σ) and particle diameter (d) determine the eddy current loss. The magnetic permeability constant in a vacuum is expressed as μ_0 [42]. The dependence of C0 on the frequency of every sample is displayed in Figure 13(a), (b). All samples have peaks at 8.5, 10.30 GHz frequencies, as Figure 13(a) illustrates, and none of them exhibit consistent behavior with frequency changes. Therefore, magnetic loss in these samples cannot be primarily caused by vortex loss. Utilizing the natural resonance equation, the resonance frequency the third factor is determined.

$$2\pi f_r = {}^{\gamma}H_a \tag{19}$$

which the gyromagnetic coefficient is:

$${}^{\gamma} = 2.8\left(\frac{GHz}{kOe}\right) \tag{20}$$

$$H_a = \frac{4|K_1|}{3\mu_0 M_s} \quad (21)$$

Considering that the anisotropy coefficient K_1 of the samples is on the order of $K_1 * 10^3$ (erg/cm^{-3}) the natural resonance frequency will be on the order of megahertz, while the observed peaks are on the order of GHz [43]. It is expected that the resonance frequency will shift to higher frequencies in nanoparticles because of the surface effect, which increases the surface anisotropy field and the value of K_1. As a result, in the nanocomposites made in this paper, magnetic resonance is the primary cause of magnetic loss. As a result, the primary influence in the nanocomposites made in this paper is magnetic loss.

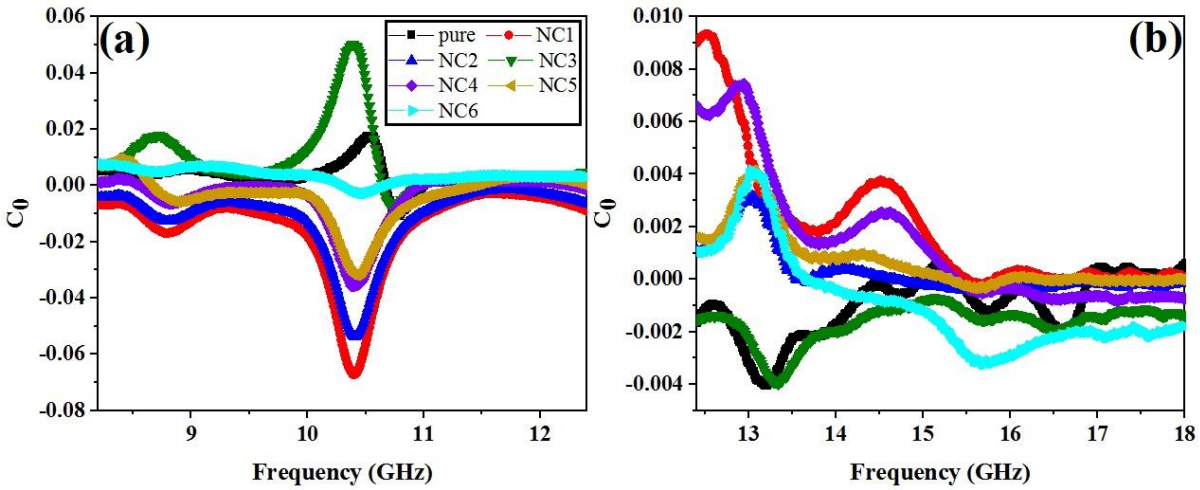

Figure 13: (A) C_0^{-f} Diagram Under the X Band, (B) C_0^{-f} Diagram Under the Ku Band.

Dielectric loss and magnetic loss are two tangent factors that affect how much microwave radiation is absorbed. Dielectric and magnetic losses are expressed as follows:

$$tan\delta_\varepsilon = \frac{\varepsilon''}{\varepsilon'} \quad (22)$$

$$tan\delta_\mu = \frac{\mu''}{\mu'} \quad (23)$$

$tan\delta_\varepsilon$ and $tan\delta_\mu$ represent dielectric losses and magnetic losses of materials to microwave energy, respectively. According to Figure 17(a), and (c), which are related to the X band, NC3 sample has the highest of $tan\delta_\mu$ and $tan\delta_\varepsilon$. Additionally, for Figure 14(b), and (d), which are related to the Ku band, NC6 sample has the highest of $tan\delta_\mu$ and $tan\delta_\varepsilon$. Therefore, it can be predicted that NC3 sample has the highest RL under the X band. The same result holds for the NC6 sample under the Ku band.

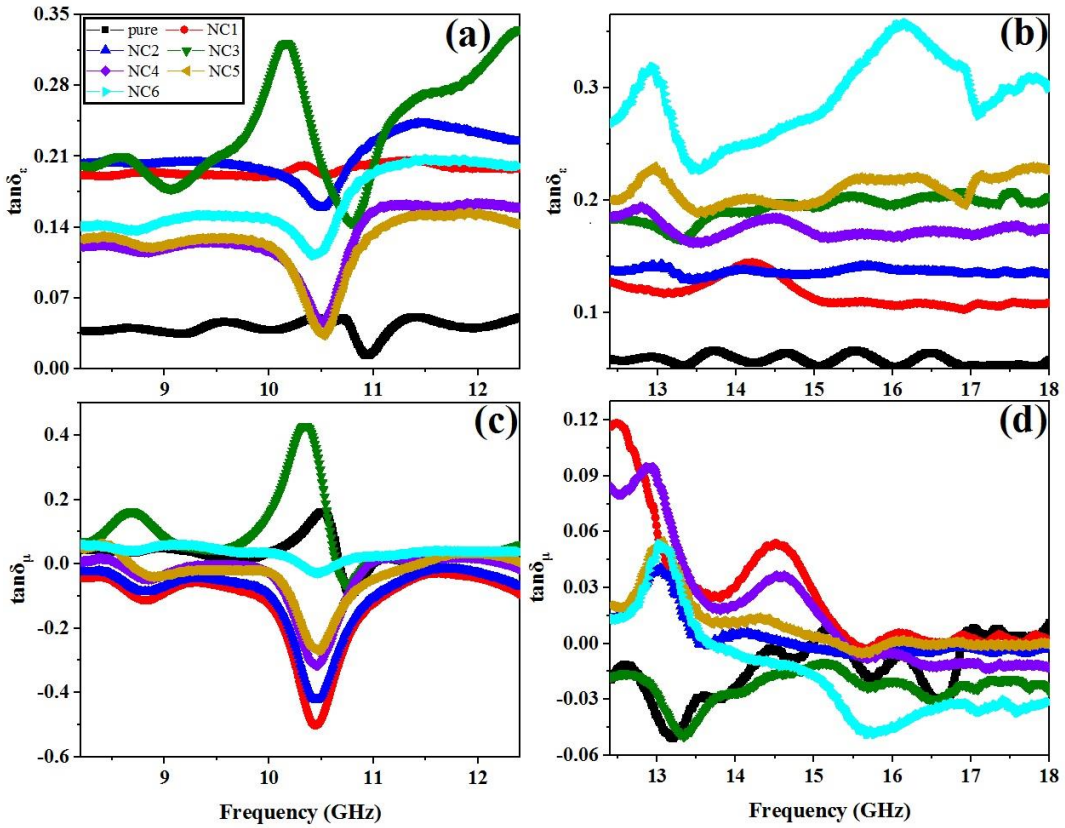

Figure 14: Diagram of (a) tanδ_{ε}, (c) tanδ_{μ} under the x Band (b) tanδ_{ε}, and (d) tanδ_{μ} under the ku Band for Pure, NC1- NC6 Samples

The following equation is used to determine the RL:

$$R_{\mathrm{L}} = 20 \ log \left|\frac{Z_{in}-Z_0}{Z_{in}+Z_0}\right| \tag{24}$$

$$Z_{in} = Z_0\sqrt{\frac{\mu_r}{\varepsilon_r}} \tanh\left(\frac{2\pi df}{C}\sqrt{\mu_r\varepsilon_r}\right) \tag{25}$$

Z_0 is the input impedance in free space (377 ohms), d is the thickness of the absorbing material, f is the frequency, and C is the speed of light. The NC3 sample under the X frequency band has the highest R_L (-27.07 dB) in the thickness of 2.25 mm under the frequency of 10.05 GHz, as expected from the results of the tangent of magnetic and dielectric losses. Furthermore, at a frequency of 16.58 GHz and a thickness of 5.00 mm, the NC4 sample exhibits the highest R_L in the Ku band (-38.21 dB). Effective loss is defined as a bandwidth with R_L less than -10 dB, or roughly 90% of EMW loss, as shown in Figure 16. Under X band, NC3, NC4, NC5, and NC6 samples have an effective loss. Furthermore, the NC3, NC4, NC5, and NC6 samples have an effective loss for the Ku band. The data show that the ultrasonic waves method produced nanocomposites with satisfactory absorption results. Furthermore, the RL values of the NC3 and NC4 samples that were simulated at various thicknesses are displayed in Figure 15c, d.

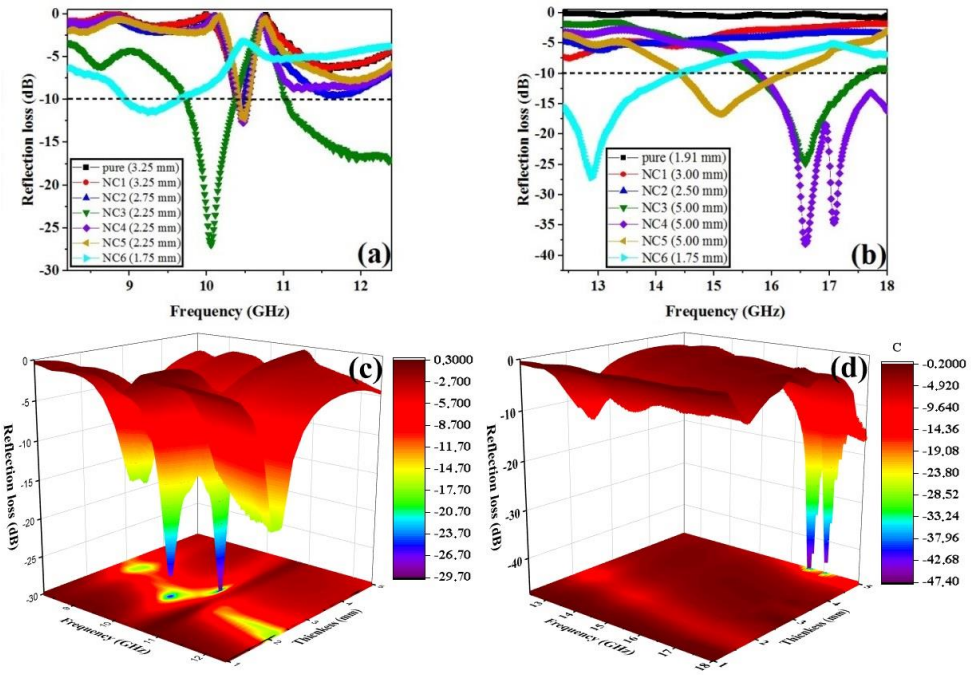

Figure 15: R_1 of Pure, NC1-NC6 Samples under (a) the X Band, (b) the Ku Band. R_L Values of (c) NC3 Sample under the X Band and, (d) NC4 Sample under the Ku Band Simulated at Different Thicknesses.

As can be seen from the relationship between mixed electrical permittivity and mixed magnetic permeability, the matched characteristic impedance plays a crucial role in the absorption behavior of the structures under discussion. Accordingly, most incident waves will be reflected from the surface if the electrical permittivity is significantly higher than the magnetic permeability, and most incident waves will pass through the object without suffering appreciable losses if the magnetic permeability is higher [44]. Stated differently, the absorption properties will be better the better the impedance matching between the surfaces, which can be determined using the following equation:

$$Z_r = \frac{Z_{in}}{Z_0}\left(\frac{\mu_r}{\varepsilon_r}\right)^{\frac{1}{2}} \tag{26}$$

The graph of Z to frequency changes for pure, NC1-NC6 samples is shown in Figure 16(a), (b). The NC3 sample has the highest impedance matching under frequency band X, as shown in the Figure Consequently, this sample had the best RL, as we have seen. Furthermore, samples NC3, NC4, NC5, and NC6 have the best impedance matching for the Ku band. The NC4 sample has the best impedance matching of all of them. that this sample has the best RL.

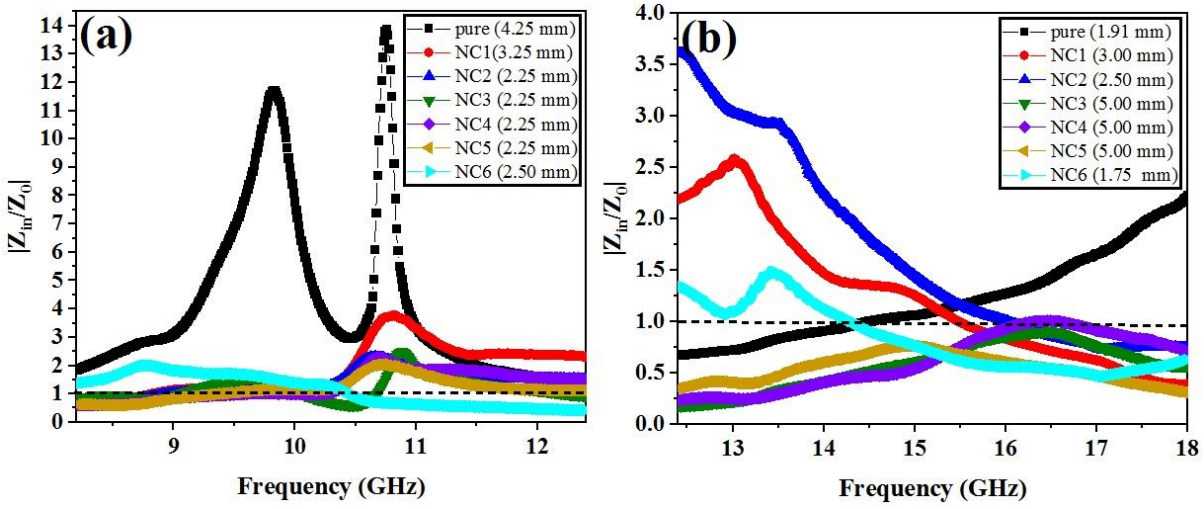

Figure 16: Impedance Matching of Pure, NC1-NC6 Samples for (A) the X Band, and (B) the Ku Band.

The attenuation coefficient determines the material's microwave absorption performance; if the impedance matching peak value is greater than 1, it indicates weak microwave RL. Impedance matching determines the microwave absorption performance of the composite; a value less than 1 indicates increased microwave reflection loss. As demonstrated in Figure 17(a), (b), samples NC3 and NC4, NC5, NC6 have optimal impedance matching under the X band and Ku band, respectively. Which demonstrates how fully the microwave waves penetrate the samples. Therefore, the attenuation coefficient determines the amount of microwave absorption of the samples. Sample NC3 has the highest attenuation coefficient under X band, as shown by Figure 18(a), (b). Furthermore, under the Ku band, the NC6 sample exhibits the highest attenuation coefficient.

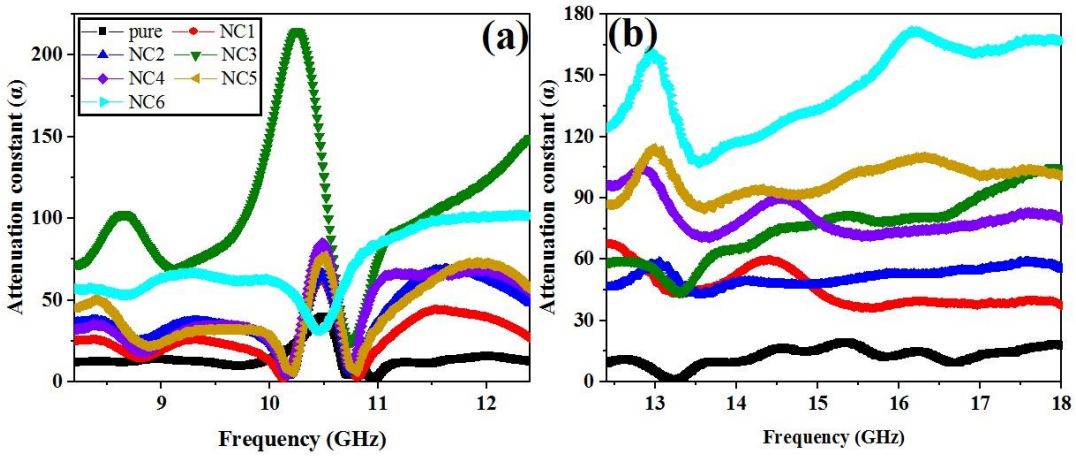

Figure 17: (A), (B) Microwave Attenuation Coefficients of Pure, NC1-NC6 Samples Under X and Ku Bands.

3.5. Microwave Absorption Optimization

A data-driven method approach is used to optimize the composition and the thickness of the microwave absorbing composites. In this method, the experimentally derived permittivity and permeability data sets are used to generate mathematical models of the electromagnetic properties (ε', ε'', μ', μ'') of a composite material as a function of additive concentration and frequency, and use these functionalized parameters for optimization purpose [45]. This method is improved to allow for multi-parameter optimization and used in this work to optimize simultaneously the composition and the thickness of the composite samples in terms of microwave absorption under the X and Ku bands [46].

Figure 18 shows 3D maps of the real and imaginary parts of complex permittivity and permeability under the X band. These maps are generated through interpolation method from measurements (red lines) and match very well the experimental results.

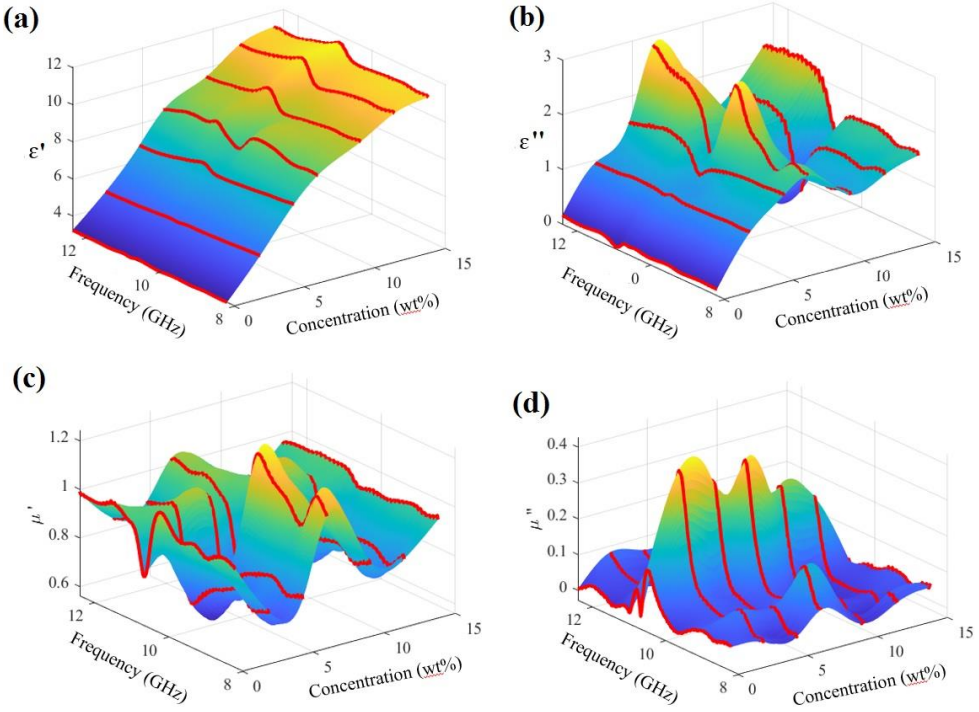

Figure 18: 3d Maps of (A) the Real Part and (B) the Imaginary Part of Complex Permittivity, and (C) the Real Part and (D) and the Imaginary Part of Complex Permeability in the X Band as Obtained by Data-Driven Method.

Using these 3D maps, it is possible to compute the reflection loss R_L for any desired CNTs concentration C (in wt%) and film thickness d. Indeed, for any given additive concentration C and sample thickness, the reflection loss can be computed as:

$$RL(C,d,f) = 20\log\left|\frac{Z_{\text{in}}(C,d,f)/Z_0 - 1}{Z_{\text{in}}(C,d,f)/Z_0 + 1}\right| \quad (27)$$

with:

$$\frac{Z_{\text{in}}(C,d,f)}{Z_0} = \sqrt{\frac{\mu_r(C)}{\varepsilon_r(C)}}\tanh\left(j\left(\frac{2\pi f d}{c}\right)\sqrt{\mu_r(C)\varepsilon_r(C)}\right) \quad (28)$$

where Z_0 and Z_{in} are the free space and the absorber impedances, respectively. Figure 19 shows color maps of the R_{Lmin} (over the considered frequency range), the effective bandwidth (EBW) and a hybrid performance parameter P, defined as following:

$$\text{RL}_{\min}(C,d) = \min_{f_{\min}\le f\le f_{\max}}\left(\text{RL}(C,d,f)\right) \quad (29)$$

$$\text{EBW}(C,d) = \sum_{\text{RL}\ge\text{RL}^{\text{thre}}}\Delta f_i \quad (30)$$

$$\text{P}(C,d) = w_1\text{RL}_{\min}(C,d) + w_2\text{EBW}(C,d) \quad (31)$$

where Δf_i is frequency step ($n\,\Delta f_i = f_{max} - f_{min}$, where n is the number of frequency points), RL^{thre} is a threshold value for absorption (= -10 dB in this work) above which the material is considered to be absorbing, and w_1 and w_2 are weights associated to the minimum rand overall bandwidth of high transmission, and are related through $w_1+w_2=1$. The parameters R_{Lmin}, EBW and P can be used to evaluate the absorption performance for any set of additive concentration and sample thickness (C, d), and thus to find out the optimal concentration and thickness (C^{opt}, d^{opt}). Namely, the lower RL_{min} and the larger the EBW, the higher will be the absorption performance of the considered sample. The weights w_1 and w_2 in the expression of the hybrid performance parameter P can be chosen based on the application of interest. Namely $w_1=1$ is adapted for applications requiring the highest absorption peak, and $w_1=0$ for applications requiring the maximum frequency range of high absorption. Intermediate values of w_1 (between 0 and 1) can be used for applications requiring the two performance parameters to be optimized simultaneously. The hybrid parameter P is normalized so that the optimum sample gives rise to a hybrid performance P = 100%. Since an ideal microwave absorbing material needs to be lightweight, the search of the optimal solution is restricted to the thickness range between 0 and 3 mm.

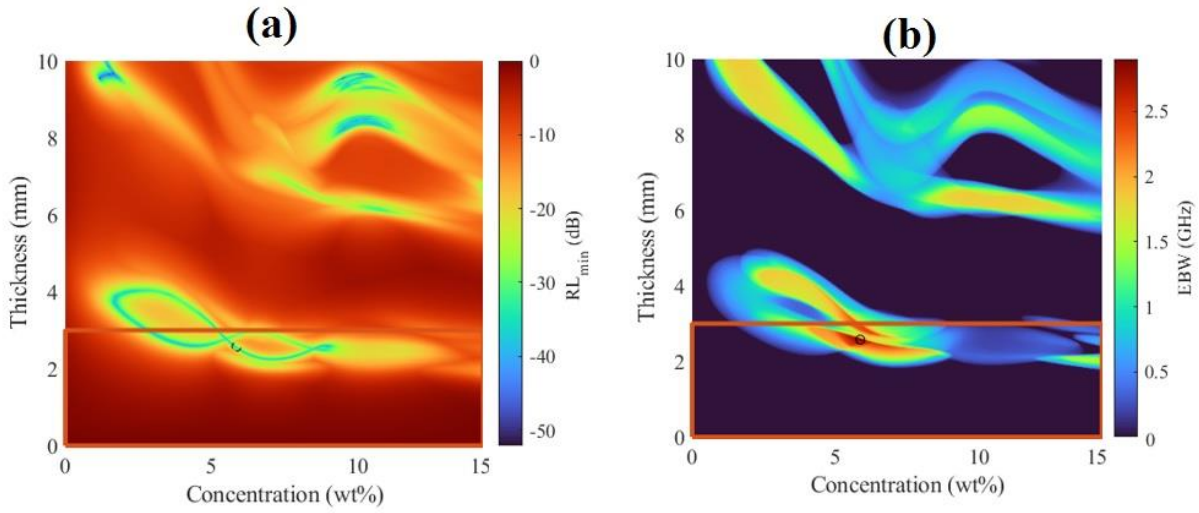

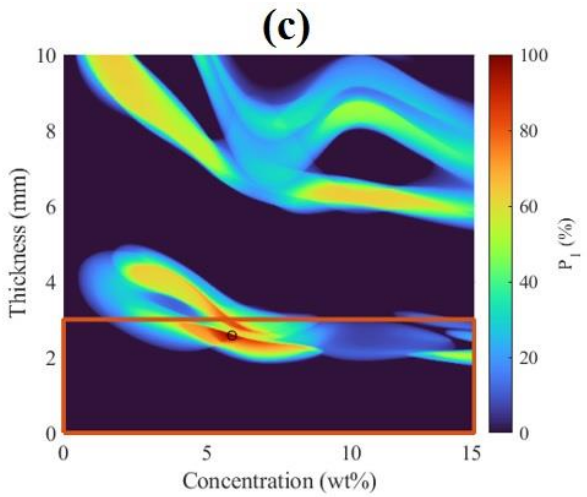

Figure 19: 3D Maps of (a) the r_{lmin}, (b) Effective Bandwidth and (c) the Performance Parameter (for the case w_1=0.5), in the X Band for Different Cnts Concentrations and Sample Thicknesses.

Figure 20 (a) shows the RL map as function of frequency and sample thickness d for the optimal concentration C^{opt} obtained in the case w_1=0.5. A comparison between the different cases, i.e. w_1=0,0.5 and 1, is shown in Figure 20(b). The optimal absorption characteristics (RLminopt, EBWopt) as obtained for the optimum solutions (C^{opt}, d^{opt}) for the different optimization goals (w_1=0,0.5 and 1) are reported in Table 3.

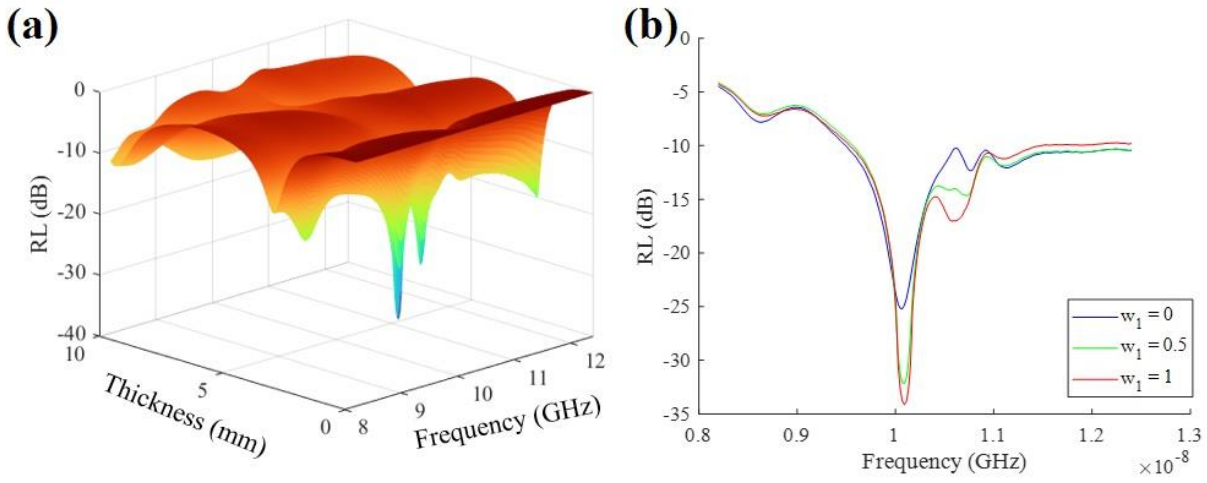

Figure 20: (a) 3D Map of R_L of the Optimum Sample in the X Band (for the case w_1=0.5). (b) Comparison of the Reflection Loss of the Optimum Samples Obtained for the Different Optimization Goals (w_1=0,1 and 2).

w1	C^{opt} (wt%)	d^{opt} (mm)	$RL_{min}{}^{opt}$ (dB)	EBW^{opt} (GHz)	EBW^{opt} (% *)
1	2.6	5.9	-25.2	2.9	69.0
0.5	2.6	5.7	-32.2	2.8	66.7
0	2.7	5.7	-34.1	1.9	45.2

Table 3: Optimum samples for the X band and their Corresponding Absorption Characteristics as Obtained for Different Optimization Goals

For the Ku band, the same procedure can be repeated, and some of the results are reported in Figure 21, Figure 22 and Table 4.

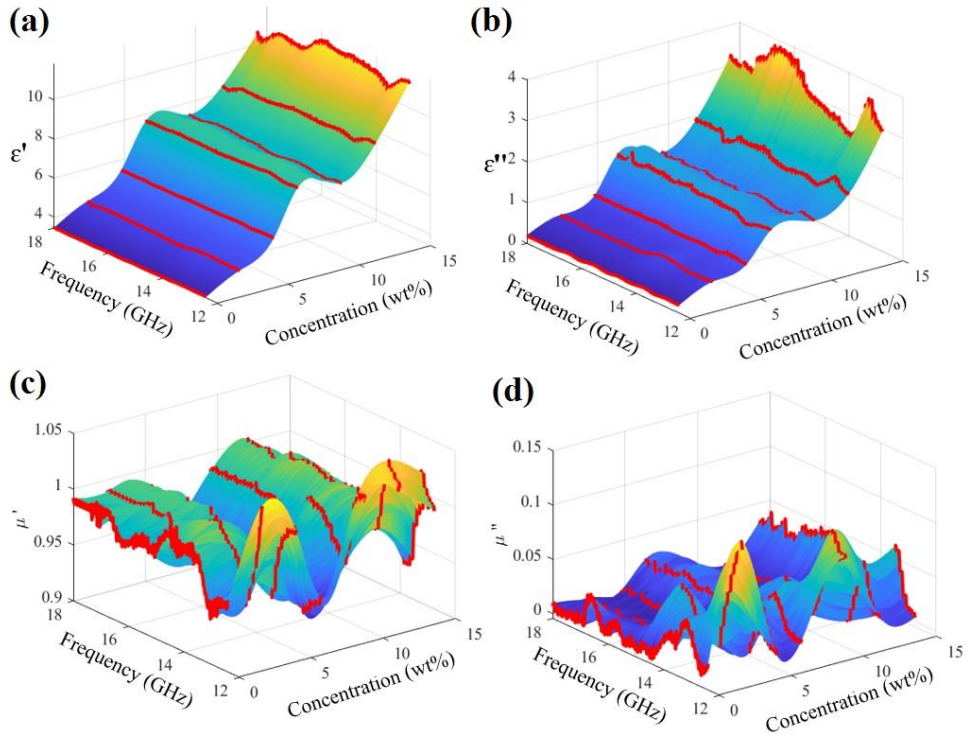

Figure 21: 3D Maps of (A) the Real Part and (B) the Imaginary Part of Complex Permittivity, and (C) the Real Part and (D) and the Imaginary Part of Complex Permeability Under the Ku-Band as Obtained By Data-Driven Method.

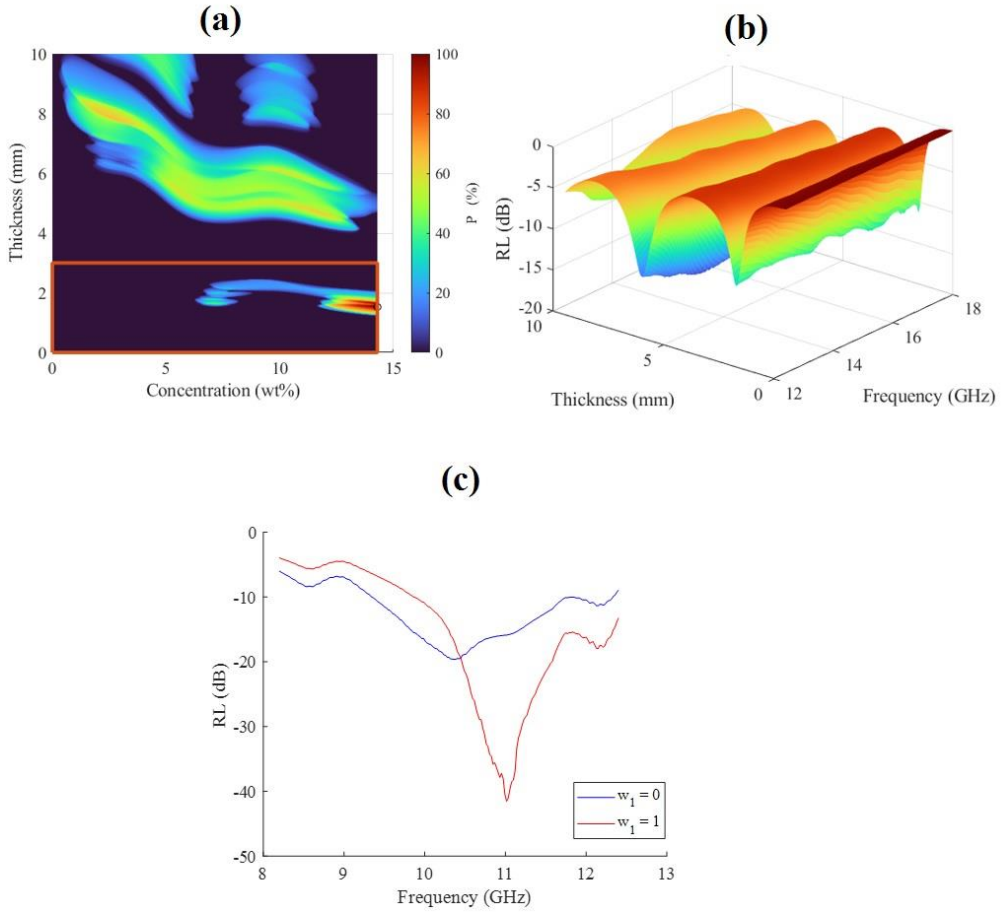

Figure 22: Data-Driven Method Results Under the Ku-Band. (a) 3d Map of the Hybrid Performance Parameter p (for the case w_1=0.5) for Different CNTs Concentrations and Sample Thicknesses. (b) 3d Map of Reflection Loss of the Optimum Sample (for the case w_1=1). (c) Comparison of the rl of the Optimum Samples Obtained for the Different Optimization Goals (w_1=0 and 1).

w_1	C^{opt} (wt%)	d^{opt} (mm)	RL_{min}^{opt} (dB)	EBW^{opt} (GHz)	EBW^{opt} (% *)
0	1.6	14.0	-19.6	4.0	71.4
1	1.5	14.0	-41.5	3.4	60.7

Table 4: Optimum samples for the Ku-Band and their Corresponding Absorption Characteristics as Obtained for Different Optimization Goals

4. Conclusion

Due to the use of both magnetic and dielectric mechanisms of absorbing microwave waves, microwave-absorbing coatings are important and have better efficiency than magnetic or dielectric absorbing materials alone. In summary, the results of XRD and FTIR analyses showed that Fe_3O_4 NPs were successfully synthesized in the cubic spinel phase without the presence of any impurities. Additionally, nanocomposites NC1, NC2, NC3, NC4, NC5 and NC6 were prepared by ultrasound. Based on the results of structural studies, it is possible to deposit high-quality Fe3O4 nanoparticles through ultrasonic waves on carbon nanotubes. As mentioned before, the dielectric properties of the samples were measured in the X and Ku frequency bands. Sample NC3 under the X frequency band has the highest RL (-27.07 dB) in the 2.25 mm thickness under the 10.05 GHz frequency. Additionally, in the Ku frequency band, sample NC4 has the highest RL (-38.21 dB) in the thickness of 5.00 mm under the frequency of 16.58 GHz. Here, the use of carbon nanotubes as dielectric materials leads to higher permeability and improved dielectric loss, which can be attributed to Debye dipole relaxation, electron polarization relaxation, and surface polarization. Therefore, the Fe3O4@ CNTs nanocomposite containing carbon nanotubes provides a new strategy for electromagnetic absorber materials due to its high potential for high capacity, lightweight, renewability, and easy mass production. A data-driven method developed for multi-parameter optimization was used to further enhance the microwave absorption performance by adjusting simultaneously the composition and film thickness. In this method, different optimization goals can be defined leading to different solutions. In particular, samples with enhanced minimum reflection loss -34.1 dB (-41.5 dB) were obtained, and other samples with enhanced effective bandwidth coving 69.0 % (71.4 %) in the X band (Ku band) were obtained. A hybrid performance parameter was also defined that allowing achieving a compromise between minimum reflection and loss effective bandwidth.

Declaration of Competing Interest

The authors declare that they have no known competing financial interests or personal relationships that could have appeared to influence the work reported in this paper.

Acknowledgments

The authors are grateful to the Imam Hossein University.

References

1. Gui, X., Wang, K., Cao, A., Wei, J., Lv, R., Kang, F., ... & Wu, D. (2010). Selective microwave absorption of iron-rich carbon nanotube composites. *Journal of nanoscience and nanotechnology, 10*(3), 1808-1813.
2. Dong, H., Chen, Y. C., & Feldmann, C. (2015). Polyol synthesis of nanoparticles: status and options regarding metals, oxides, chalcogenides, and non-metal elements. *Green chemistry, 17*(8), 4107-4132.
3. Lu, B., Dong, X. L., Huang, H., Zhang, X. F., Zhu, X. G., Lei, J. P., & Sun, J. P. (2008). Microwave absorption properties of the core/shell-type iron and nickel nanoparticles. *Journal of magnetism and magnetic materials, 320*(6), 1106-1111.
4. Tang, R., Li, T., Wu, Z., Cai, W., Jiang, H., Yang, Z., ... & Yu, R. (2011). Magnetic and Microwave Absorption Properties of Core/Shell FeCo-Based Nanocomposites Synthesized by a Simple Wet Chemical Method. *IEEE transactions on magnetics, 47*(10), 3456-3459.
5. Gogoi, J. P., Bhattacharyya, N. S., & Bhattacharyya, S. (2014). Single layer microwave absorber based on expanded graphite–novolac phenolic resin composite for X-band applications. *Composites Part B: Engineering, 58*, 518-523.
6. Li, D., Feng, Y., Pan, D. S., Jiang, L. W., Dai, Z. M., Li, S. J., ... & Zhang, Z. D. (2016). Negative imaginary parts of complex permeability and microwave absorption performance of core double-shelled FeCo/C/Fe2. 5Cr0. 5Se4 nanocomposites. *RSC advances, 6*(77), 73020-73027.
7. Yang, H., Ye, T., Lin, Y., & Liu, M. (2015). Exchange coupling behavior and microwave absorbing property of the hard/soft (BaFe12O19/Y3Fe5O12) ferrites based on polyaniline. *Synthetic Metals, 210,* 245-250.
8. Zhao, B., Shao, G., Fan, B., Xie, Y., & Zhang, R. (2014). Preparation and electromagnetic wave absorption of chain-like CoNi by a hydrothermal route. *Journal of magnetism and magnetic materials, 372*, 195-200.
9. Che, R. C., Zhi, C. Y., Liang, C. Y., & Zhou, X. G. (2006). Fabrication and microwave absorption of carbon nanotubes/CoFe2O4 spinel nanocomposite. *Applied Physics Letters, 88*(3).
10. Zhao, D. L., Zhang, J. M., Li, X., & Shen, Z. M. (2010). Electromagnetic and microwave absorbing properties of Co-filled carbon nanotubes. *Journal of Alloys and Compounds, 505*(2), 712-716.
11. Qing, Y. C., Zhou, W. C., Jia, S., Luo, F., & Zhu, D. M. (2010). Electromagnetic and microwave absorption properties of carbonyl iron and carbon fiber filled epoxy/silicone resin coatings. *Applied Physics A, 100,* 1177-1181.
12. Tong, G., Wu, W., Hua, Q., Miao, Y., Guan, J., & Qian, H. (2011). Enhanced electromagnetic characteristics of carbon nanotubes/carbonyl iron powders complex absorbers in 2–18 GHz ranges. *Journal of Alloys and Compounds, 509*(2), 451-456.
13. Ji, X., Lu, M., Ye, F., & Zhou, Q. (2012). Microwave absorption properties of flake graphite and carbonyl-iron particles filled aliphatic polyurethane resin. *Adv Mech Eng Appl, 3,* 294-298.
14. Ji, X., Lu, M., Ye, F., & Zhou, Q. (2013). Preparation and re-

search on the electromagnetic wave absorbing coating with Co-ferrite and carbonyl iron particles. *Journal of Materials Science Research, 2*(2), 35.
15. Zhou, Y., Zhou, W., Qing, Y., Luo, F., & Zhu, D. (2015). Temperature dependence of the electromagnetic properties and microwave absorption of carbonyl iron particles/silicone resin composites. *Journal of Magnetism and Magnetic Materials, 374*, 345-349.
16. Cui, C., Du, Y., Li, T., Zheng, X., Wang, X., Han, X., & Xu, P. (2012). Synthesis of electromagnetic functionalized Fe3O4 microspheres/polyaniline composites by two-step oxidative polymerization. *The Journal of Physical Chemistry B, 116*(31), 9523-9531.
17. Liu, P., Huang, Y., Yang, Y., Yan, J., & Zhang, X. (2016). Sandwich structures of graphene@ Fe3O4@ PANI decorated with TiO2 nanosheets for enhanced electromagnetic wave absorption properties. *Journal of Alloys and Compounds, 662,* 63-68.
18. Taufiq, A., Sutiami, R., Subadra, S. U., Hidayat, A., Diantoro, M., Sunaryono, S., ... & Adi, W. A. (2020). Radar absorption performance of Fe3O4/AC/PANI nanocomposites prepared from natural iron sand. *International Journal of Engineering, 33*(2), 304-313.
19. Jiang, Q., Li, H., Cao, Z., Li, H., Wang, Q., Jiang, Z., ... & Xie, Z. (2017). Synthesis and enhanced electromagnetic wave absorption performance of amorphous CoxFe10-x alloys. *Journal of Alloys and Compounds, 726,* 1255-1261.
20. Z Wu, Z., Tan, D., Tian, K., Hu, W., Wang, J., Su, M., & Li, L. (2017). Facile preparation of core–shell Fe3O4@ Polypyrrole composites with superior electromagnetic wave absorption properties. *The Journal of Physical Chemistry C, 121*(29), 15784-15792.
21. Su, X., Wang, J., Zhang, B., Chen, W., Wu, Q., Dai, W., & Zou, Y. (2018). Enhanced microwave absorption properties of epoxy composites containing graphite nanosheets@ Fe3O4 decorated comb-like MnO2 nanoparticles. *Materials Research Express, 5*(5), 056305.
22. He, Z., Fang, Y., Wang, X., & Pang, H. (2011). Microwave absorption properties of PANI/CIP/Fe3O4 composites. *Synthetic Metals, 161*(5-6), 420-425.
23. Cui, C., Du, Y., Li, T., Zheng, X., Wang, X., Han, X., & Xu, P. (2012). Synthesis of electromagnetic functionalized Fe3O4 microspheres/polyaniline composites by two-step oxidative polymerization. *The Journal of Physical Chemistry B, 116*(31), 9523-9531.
24. Chikazumi, S. (1997). Physics of ferromagnetism (No. 94). Oxford university press.
25. Beyranvand, M., & Gholizadeh, A. Structural, magnetic, elastic and dielectric properties of.
26. Gholizadeh, A. (2017). A comparative study of physical properties in Fe3O4 nanoparticles prepared by coprecipitation and citrate methods. *Journal of the american ceramic society, 100*(8), 3577-3588.
27. Gholizadeh, A., & Beyranvand, M. (2020). Structural, magnetic, elastic, and dielectric properties of Mg0. 3− xBaxCu0. 2Zn0. 5Fe2O4 nanoparticles. *Physica B: Condensed Matter, 584,* 412079.
28. Beyranvand, M., & Gholizadeh, A. (2020). Structural, magnetic, elastic, and dielectric properties of Mn0. 3− x Cd x Cu0. 2Zn0. 5Fe2O4 nanoparticles. *Journal of Materials Science: Materials in Electronics, 31*(7), 5124-5140.
29. Gholizadeh, A., & Beyranvand, M. (2020). Investigation on the structural, magnetic, dielectric and impedance analysis of Mg0. 3-xBaxCu0. 2Zn0. 5Fe2O4 nanoparticles. *Physica B: Condensed Matter, 584*, 412079.
30. Saleh, T. A., Gondal, M. A., Drmosh, Q. A., Yamani, Z. H., & Al-Yamani, A. (2011). Enhancement in photocatalytic activity for acetaldehyde removal by embedding ZnO nano particles on multiwall carbon nanotubes. *Chemical Engineering Journal, 166*(1), 407-412.
31. Safari, J., & Gandomi-Ravandi, S. (2014). Fe 3 O 4–CNTs nanocomposites: a novel and excellent catalyst in the synthesis of diarylpyrimidinones using grindstone chemistry. *RSC Advances, 4*(22), 11486-11492.
32. Mallakpour, S., & Zadehnazari, A. (2014). A facile, efficient, and rapid covalent functionalization of multi-walled carbon nanotubes with natural amino acids under microwave irradiation. *Progress in Organic Coatings, 77*(3), 679-684.
33. Liu, S., Mei, L., Liang, X., Liao, L., Lv, G., Ma, S., ... & Xi, K. (2018). Anchoring Fe3O4 nanoparticles on carbon nanotubes for microwave-induced catalytic degradation of antibiotics. *ACS applied materials & interfaces, 10*(35), 29467-29475.
34. Manna, K., & Srivastava, S. K. (2017). Fe3O4@ carbon@ polyaniline trilaminar core–shell composites as superior microwave absorber in shielding of electromagnetic pollution. *ACS Sustainable Chemistry & Engineering, 5*(11), 10710-10721.
35. Wu, W., Jiang, C. Z., & Roy, V. A. (2016). Designed synthesis and surface engineering strategies of magnetic iron oxide nanoparticles for biomedical applications. *Nanoscale, 8*(47), 19421-19474.
36. Kulkarni, S. A., Sawadh, P. S., Palei, P. K., & Kokate, K. K. (2014). Effect of synthesis route on the structural, optical and magnetic properties of Fe3O4 nanoparticles. *Ceramics International, 40*(1), 1945-1949.
37. Yang, J., Zou, P., Yang, L., Cao, J., Sun, Y., Han, D., ... & Kong, X. (2014). A comprehensive study on the synthesis and paramagnetic properties of PEG-coated Fe3O4 nanoparticles. *Applied Surface Science, 303,* 425-432.
38. Cao, J., Liu, Q., Du, J., Yang, L., Wei, M., Gao, M., & Yang, J. (2017). Facile one-step hydrothermal method to fabricate Fe 3 O 4 quantum dots–graphene nanocomposites for extraction of dye from aqueous solution. *Journal of Materials Science: Materials in Electronics, 28*, 2267-2271.
39. Ashiq, M. N. (2009). Effect on Physical, Electrical and Magnetic Properties of Strontium Hexaferrite Nanomaterial Doped with Binary Mixtures of Various Metal Ions (Doctoral dissertation, Quaid-i-Azam University Islamabad, Pakistan).
40. Ashiq, M. N., Iqbal, M. J., Najam-ul-Haq, M., Gomez, P. H., & Qureshi, A. M. (2012). Synthesis, magnetic and dielectric properties of Er–Ni doped Sr-hexaferrite nanomaterials for applications in High density recording media and microwave devices. *Journal of magnetism and magnetic materials, 324*(1), 15-19.

41. Shamgani, N., & Gholizadeh, A. (2019). Structural, magnetic and elastic properties of Mn0. 3− xMgxCu0. 2Zn0. 5Fe3O4 nanoparticles. *Ceramics International, 45*(1), 239-246.
42. Lu, B., Dong, X. L., Huang, H., Zhang, X. F., Zhu, X. G., Lei, J. P., & Sun, J. P. (2008). Microwave absorption properties of the core/shell-type iron and nickel nanoparticles. *Journal of magnetism and magnetic materials, 320*(6), 1106-1111.
43. Hall, R. C. (1959). Single crystal anisotropy and magnetostriction constants of several ferromagnetic materials including alloys of NiFe, SiFe, AlFe, CoNi, and CoFe. *Journal of Applied Physics, 30*(6), 816-819.
44. Xu, P., Han, X., Wang, C., Zhou, D., Lv, Z., Wen, A., ... & Zhang, B. (2008). Synthesis of electromagnetic functionalized nickel/polypyrrole core/shell composites. *The Journal of Physical Chemistry B, 112*(34), 10443-10448.
45. Green, M., Van Tran, A. T., & Chen, X. (2020). Maximizing the microwave absorption performance of polypyrrole by data-driven discovery. *Composites Science and Technology, 199,* 108332.
46. S.M.B. Bahrani, E. Mohammadi, S.M. Masoudpanah, S.S. Seyyed Afghahi, A.A. Ebrahimi Valmoozi, (2023) "A modified data-driven optimization method for obtaining strong broadband microwave transparent Si3N4/BAS/BN composites" (under publication).